Aalto University
School of Electrical
Engineering

Imaya Senthilnathan

Surface analysis of Detonation Nanodiamond thin films fabricated using automated spray coating technique

Thesis submitted for examination for the degree of Master of Science in Technology.

Espoo 23.04.2018

Thesis supervisor: Prof. Tomi Laurila

Thesis advisor: D.Sc (Tech.) Sami Sainio

Author Imaya Senthilnathan

Title of thesis Surface analysis of Detonation Nanodiamond thin films fabricated using automated spray coating technique

Degree programme Master's Programme in Automation and Electrical Engineering

Major Translational Engineering **Code** ELEC3023

Thesis supervisor Prof. Tomi Laurila

Thesis advisor(s) D.Sc. (Tech.) Sami Sainio

Date 23/04/2018 **Number of pages** 61+8 **Language** English

Abstract

In recent years, Detonation Nanodiamond (DND) has gained importance as a biomaterial. DND can be made into thin film coating on substrates, which is a requirement for many bioanalytical sensing devices. In this work, the distribution and thickness of DND coated as thin film on silicon substrate were studied. The coating was performed using an automated spray coating device designed for thin film deposition. The spray coated samples were compared with samples fabricated by spin coating. Scanning Electron Microscopy (SEM) was used as the analysis tool to analyse the distribution and thickness of the thin film samples.

DNDs were observed as densely packed agglomerates on the surface of the thin film coatings. Agglomeration causes the DND particles to form clusters resulting in unevenness of coating surface. To prevent agglomeration and improve evenness of coating, deagglomeration is carried out using ultrasonication. The core aggregates were left intact, and the smallest observable aggregates were no less than 10nm. The thickness of DND coated thin films was measured using SEM. Thickness measurements show the coating to be uneven, which is expected to occur due to agglomeration. The average thickness of spray coating samples lies between 450 – 550 nm and that of spin coated samples lie between 200-300 nm for the same amount of solution consumption per unit area. Delamination of DND coating from Silicon substrate occurred due to the intense grinding and polishing processes during sample preparation for SEM analysis, which decreases the evenness of coating and accuracy of measurements. Improved sample preparation methods are required to obtain accurate thickness measurement using SEM.

Further improvements on deagglomeration techniques might improve the distribution of DND particles, and consistency of coating thickness in DND thin film coatings. SEM has resolution power in the nanometre scale making it a good analysis tool to measure the distribution of the thin film coatings. Nevertheless, it was not possible to observe primary DND particles with good resolution below 100 nm scale using SEM. SEM along with improved sample preparation methods could possibly be a good analysis tool for thickness measurements, as it is required to fabricate measurable and repeatable thin film coatings in industrial scale.

Keywords Detonation Nanodiamond, Thin film coatings, Scanning electron microscopy, Surface analysis, Coating thickness

Preface

I would like to thank professor Tomi Laurila for giving me the opportunity to work on this thesis. I would like to thank my advisor Sami Sainio for his valuable guidance in helping me write this thesis. I would like to thank my family and friends, who has always been a great support to me through thick and thin. Finally, I would like to thank Aalto university and Finland for accepting me into the country and the educational community, and making it possible for me to pursue my studies.

Espoo, 13.04.2018,

Imaya Senthilnathan

Contents

Abstract iii
Preface ivii
Contents iiv
Abbreviations ivi
1 Introduction 1
2 Nanodiamond thin films 3
3 Detonation Nanodiamonds 4
3.1 Historical Background 4
3.2 Classification of Nanodiamonds 4
3.3 Structure of DND 6
3.3.1 Lattice structure 6
3.3.2 Surface structure 6
3.2 Detonation synthesis 8
3.2.1 Mechanism of formation of DND 8
3.3 Post synthesis purification of DND 10
3.4 Surface functionalization 13
4 Agglomeration in DND 15
4.1 Mechanism of agglomeration 16
4.2 Mechanical deagglomeration 17
4.2.1 Centrifugation 17
4.2.2 Bead milling 18
4.2.3 Bead assisted sonic disintegration 18
5 DND Biocompatibility 20
5.1 Biocompatibility and cytotoxicity studies 20
5.2 DND thin films - biomedical applications 22
5.2.1 DNA immobilization for the fabrication of biologically active ND thin film substrates 22
5.2.2 Biosensor for the electrochemical detection of neurotransmitters using ND electrodes: 23
5.2.3 DNDs as electrochemical sensors 23
5.2.4 Immobilization of antibodies and bacterial binding on nanodiamond – biosensing: 24
6 Thin film coatings 25
6.1 Spin coating 27
6.2 Spray coating 28

6.3 Automated spray coating technique 29
6.3.1 Movement control 29
6.3.2 Spray system 30
6.3.3 Electronics and programming 31
7 Scanning Electron Microscopy 33
7.1 Introduction 33
7.2 SEM – Subsystems 34
7.3 Factors influencing image quality 36
7.4 High resolution imaging at low voltage 36
8 Experimental part 38
8.1 Spin coating 38
8.2 Automated spray coating 38
8.3 Sample preparation for SEM analysis 38
8.3.1 Cross-section preparation 38
8.3.2 Sputter coating 39
9 Results 40
9.1 Distribution 40
9.2 Agglomeration 41
9.2.1 Size distribution 41
9.2.2 Observation of primary particles 42
9.3 Thickness measurement 44
10 Discussion 46
11 Conclusion 50
Acknowledgement 51
References 52
Appendix 61

Abbreviations

AFM	Atomic Force Microscopy
BDD	Boron Doped Diamond
BSE	Backscattered electrons
CB	Carbon Black
CNF	Carbon Nanofibre
CNT	Carbon Nanotube
CVD	Chemical Vapor Deposition
DLC	Diamond-like Carbon
DNA	Deoxyribonucleic acid
DND	Detonation Nanodiamond
EPD	Electrophoretic deposition
FIB	Focused Ion Beam
HNO_3	Nitric Acid
H_2O_2	Hydrogen Peroxide
HPHT	High Pressure High Temperature
H_2SO_4	Sulfuric Acid
$K_2Cr_2O_7$	Potassium Dichromate
KNO_3	Potassium Nitrate
MTT	(3-(4,5-dimethylthiazol-2-yl)-2,5-diphenyltetrazolium bromide)
MWCNT	Multi-Walled Carbon Nanotube
MWCVD	Micro Wave Chemical Vapor Deposition
NCD	Nano Crystalline Diamond
ND	Nanodiamond
PECVD	Plasma Enhanced Chemical Vapor Deposition
PMMA	Poly (methyl methacrylate)
PTFE	Polytetrafluoroethylene
RDX	hexahydro-1,3,5-trinitro-1,3,5-triazine
RFCVD	Radio Frequency Chemical Vapor Deposition

ROS	Reactive Oxygen Species
SE	Secondary electrons
SEM	Scanning Electron Microscope
SWCNT	Single-walled Carbon Nanotube
ta-C	Tetrahedral Amorphous Carbon
TEM	Transmission Electron Microscope
TNT	2-methyl-1,3,5-trinitrotouluene
UNCD	Ultra Nano Crystalline Diamond
WST	Water-soluble tetrazolium salt
XTT	((2,3-bis-(2-methoxy-4-nitro-5-sulfophenyl)-2H-tetrazolium-5-carboxanilide)

1 Introduction

With the advancement of technology over the past few decades, the interdependence between various disciplines of engineering like biotechnology, material science and chemistry has led to the production of a wide variety of biosensing devices [1]. They are used in applications such as bioanalytical studies, biomedical probing, enzymatic, nucleic acid and other biological interactions, and microbial biosensing [2, 3]. They are composed of two components, the biological component and the physicochemical detection component. The 'biomaterial' which is used as the detection component can be broadly classified as inert, bioactive and biodegradable/bio-resorbable. Most biosensors require biomaterials to be bioactive [4]. Bioactive materials stimulate tissue growth by enhancing bonding to the tissue. These biomaterials invariably react with cells and tissues to collect the desired information, whether *in vitro* or *in vivo*. Such biomaterials are required to be biocompatible and should work in wide range of pH and temperature conditions with high sensitivity and functionality [5].

Carbon materials have gained traction for use in bio-applications due to their unique electrical, chemical, mechanical and optical properties. The family of carbon structures include carbon nanotubes (CNT), glassy carbon, carbon fibres and graphene, diamond like carbon (DLC), carbon nanofibres (CNF), boron doped diamond (BDD), carbon black (CB) and tetrahedral amorphous Carbon (ta-C) which have been used extensively in bio-applications [1, 6, 7]. Detonation nanodiamonds (DND) belonging to this family have been researched as suitable candidates for bio-applications [1, 8-12]. DNDs are suitable materials for thin film biosensing applications, because of their nanostructure, large surface area and surface to volume ratio, high stability, chemical inertness, bio-inertness, high Young's modulus and biocompatibility. Many bio-applications including immobilization of proteins, enzymes, antibodies and DNA [8], and electrochemical biosensors detecting electrochemically active bio-substances [13], have used DND coated thin film substrate as their sensor material [14].

The coating of DND thin films on surfaces for bio-applications is achieved by methods like spray coating [15], spin coating [16], electrophoretic deposition [17] and dip coating [18]. Spray coating and spin coating methods are used in the experimental part of the thesis. They are less complicated as they do not require strict instrumentation and gaseous waste treatments. They are also less time consuming and provide coating thickness control. Besides these factors, the coating technique should also satisfy requirements like reliability, repeatability, consistency and speed of fabrication [20].

Topological parameters are important aspects in the analysis of such thin film coatings. The ever-reducing size of the biosensors demand surfaces with controllable thickness in the micro and nano scale. Materials like DND exist in powder form and it is desirable to coat them as thin films on substrates for many biological applications [10-12]. The *thickness* of the surface coating and the *distribution* of the coating material on the sensor surface define the physicality of the thin film coating on the sensor surface [20]. They also affect the functionality of the biosensor. For example, to improve the sensitivity of a biosensor towards a target analyte, it is desirable to produce controllable and densely packed nanostructures as thin films along with increased density of functional groups, that enable large number of reaction sites for the target analytes [7, 10, 20].

Various methods are available to visually study the physical parameters of thin film coatings including scanning electron microscopy (SEM), transmission electron microscopy (TEM) and optical microscopy. SEM is one of the most widely used tools for microstructural analysis and surface properties investigation, especially in the investigation of topological features [20]. It has many advantages for such analyses [22] like magnification down to the nanoscale, high resolution, multiple signal generation providing information about various facets of surface topology, simple image formation process and excellent depth of field. TEM surpasses the magnification and resolution power of SEM. However, SEM has the advantages of lower cost, less complicated sample preparation and less time consumption, making it the optimal choice for surface topological imaging and analysis [20, 22].

In this thesis, DND thin films are coated on silicon substrates using an automated spray coating technique. The technique involves the use of a '3D printer' base to automate the spray coating process, by using corresponding software. These samples are analysed for surface topological parameters which include thickness of the coating and distribution of the coating material, in order to evaluate the effectiveness of the thin film coatings. The analyses are done using micrographs obtained using SEM. The results are also compared to the samples fabricated using spin coating method.

2 Nanodiamond thin films

Carbon nanostructures are widely being regarded as suitable materials for biological and biomedical applications. This is due to their unique physical, electronic, and mechanical properties along with biocompatibility, high active surface areas, docking sites for redox reactions, ease of functionalization, maintenance of functionality over extended time and sensitivity [2, 24]. DNDs belonging to the family were discovered several decades ago, but they were not studied extensively until the last decade for their use in biomedical applications [1, 14].

Biosensors are used extensively in biomedical applications like diagnosis of infectious diseases, glucose biosensing, immuno-sensing, neurochemical detection, and detection of cancer markers [2]. The detector part of the biosensor plays an important role in the quality of the sensor. The material of the detector surface interacts with the biological component or the analyte and determines the output of the sensor. The characteristics of this biomaterial becomes vital in the biological component - detector material interactions [25]. DNDs have shown potential to be suitable biomaterial [6, 8, 11, 12, 26] because of their narrow size distribution, biocompatibility, and facile surface functionalization. In addition, DNDs can also be made into thin film coatings on substrates, which is an important requirement for many bioanalytical sensing devices.

In the field of biomedical engineering, DND thin films are used in several applications. DND thin films are used to immobilize DNA to biosensor that can be used to detect genetic and infectious diseases [8]. They are also used in protein immobilization biosensors for enzymatic analysis [9], and antibody immobilization biosensors used in the detection of variuos antigens and microbes [12, 27]. Nanodiamond surfaces have also shown to promote neuronal growth and adhesion and provides good platform supporting cell growth [18]. The redox activity demonstrated by DND coated electrodes have opened possibilities for DNDs as electrode materials in electrochemical sensors [28-31]. ND thin film coatings are also used in coating of certain components of artificial heart valves and dental implants [20]. Apart from biomedical applications, DNDs are used as composites with metals and polymers to produce wear resistant thin film coatings along with improved hardness, corrosion resistance and reduced porosity [7, 32]. Further investigation of DND thin films, and the fabrication and analysis of homogeneous DND thin film is required for them to be extensively used in abovementioned applications.

3 Detonation Nanodiamonds

3.1 Historical Background

NDs belong to the family of nanocarbons. These nanocarbons have diamond structures belonging to the nanoscale (~1-100nm), and carbon as their building block. They include diamond particles, 1D nanorods, 2D nanoplatelets, pure-phase diamond films and ultra-nanocrystalline diamonds. The Ultra Nanocrystalline diamonds (UNCD) which include DNDs, contain individual units over a range of just a few nanometres, the average size typically around 4.5 nm and are structurally and characteristically distinguished from other diamond nanostructures that have characteristic sizes above ~10 nm [7, 34-37].

The events that led to the discovery of DNDs were set forth by the attempt to synthesize diamond by using shock waves over carbon-based source material [38]. In mid 1960s, DuPont et.al. invented a standard to synthesize and process DNDs using the same method. Between the 1960s and 1980s several research groups carried out independent work on detonation synthesis of nanodiamonds in Russia (Volkov & Danilenko, Staver et.al.) [39] and the US (Adadurov et.al.) [40]. It is known that the synthesis of nanodiamonds was discovered over three times in 19 years, between 1963 and 1982, while three different groups were studying diamond synthesis with non-diamond carbon modifications in blast chambers [36].

3.2 Classification of Nanodiamonds

Nanodiamond powders are classified into different catagories based on their primary particle size, namely, Nanocrystalline diamond particulate, ultrananocrystalline diamond particulate, higher diamondoids, lower diamondoids. Currently there are several commercial centres to produce DND including locations in Russia, Ukraine, China and Japan [41]. The size-based classification of nanoscale diamond is given in Table 1.

Table 1: *Classification of nanodiamonds based on primary particle size [7, 37].*

Types of nanoscale diamond particles	Sub types	Primary particle size	Manufacturing Methods
Nano Crystalline Diamond Particulate	Monocrystalline	10-100nm	Natural Synthetic - High Pressure - High Temperature (HPHT)
	Polycrystalline	0-50nm	Shock wave compression of graphite (DuPont process)
Ultra-Nanocrystalline Diamond Particulate	-	0-10nm	Detonation synthesis Vapor grown Chlorination of carbide Ion irradiation of graphite
Higher Diamondoids	-	1-2nm	Isolated from petroleum
Lower Diamondoids	-	A few 10s to 100s of carbon atoms	Extracted from crude oil

NCD particles exist in monocrystalline and polycrystalline forms or a mix of both (most stable). They have primary particle range from few to tens of nanometers. They occur naturally as the purest form of nanodiamonds [37] or are manufactured by grinding of micro diamond particles.

UNCD particles are manufactured by detonation synthesis, vapour grown deposition, chlorination of carbide and ion irradiation of graphite. Of these, DNDs produced by detonation synthesis are commercially successful. DNDs have an average size between 2 to 10 nm [1, 7, 11, 14]. DND has remained the most popular candidate among the family of diamond nano-particles for biomedical applications [7].

Diamondoids contain higher diamondoids and lower diamondoinds. Higher diamondoids are 1-2 nm sized diamond species that are hydrogen-terminated. They exist in size range as an intermediate between a single adamantane molecule (the smallest species of H-terminated cubic diamond with 10 carbon atoms) and UNDC particles of sizes more than ~2nm [37]. Lower diamondoids include adamantane, diadamantane and triadamantane and are extracted from crude oil. Derivatives of adamantane like $C_{10}H_{16}$ have been used as viable candidates in biosensing and biomedical applications [36, 42].

3.3 Structure of DND

3.3.1 Lattice structure

The structure, composition, size and shape of DNDs are influenced by the technique and purification methods related to detonation synthesis. There is various lattice structures, shapes and sizes of detonation nanodiamonds [43]. The most commonly found are well faceted polyhedral, truncated octahedral, spherical and cuboctahedral particles (see Figure 1). DND surface can be represented by the arrangement of two distinct crystallographic planes (111) and (1000) [44]. The truncated octahedron is composed of 76% of (111) planes and 24% of (100). The cuboctahedron has the composition of 36% of (111) planes and 64% of (100) planes [7]. The size distribution of nanodiamonds obtained by detonation synthesis varies between 2-10 nm [7, 32, 37, 43].

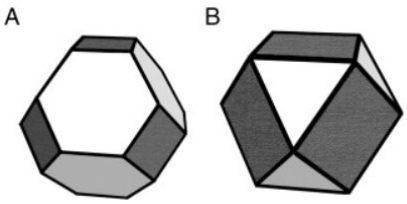

Figure 1: *Truncated octahedron and cuboctahedron structures of DND – representative [44]*.

3.3.2 Surface structure

At the nanoscale, material properties are influenced differently by the surface atoms and atoms below the surface. The number of surface atoms increase with decreasing particle size. For particles of size 2-6 nm, around 20-30% of atoms are present in the surface, and each possess at least one unsaturated dangling bonding site. Since the presence of these sites are energetically unfavourable and highly reactive, most of them reconstruct, thus saturating the bonds and forming fullerene-like structures. The reconstruction causes the formation of π-bonds which results in the sp^2-hybridization of the surface atoms. Such particles with sp^2-hybridized surface and sp^3-hybridized core, with unsaturated bonding sites in-between them are called ‘bucky’ diamonds. They are stable and commonly found. However, an unstructured amorphous carbon outer layer containing a mixture of sp^2 and sp^3 carbons are also reported in some studies [7].

The structure of DND is greatly influenced by the synthesis mechanisms. With changes in the steps involved in the synthesis and purification processes, the DND structural properties tend to vary. However, the most widely accepted structure of DND contains a core, a carbon shell around the core and functional groups surrounding the surface [7, 34].

- The *core* contains sp^3- hybridized carbon, like bulk diamond. The size of the core can vary between 2-6nm in diameter and contains majority of the carbon atoms (see Figure 2) [34, 45].

- The *outer carbon shell* contains 10-30% of carbon atoms and has between 4-10 Å. Two widely accepted models for the outer shell include bucky diamond with sp^2 hybridized fullerene shell, and unstructured amorphous carbon containing both sp^2 and sp^3 hybridized carbon atoms [34, 45].
- A wide variety of *functional groups* cover the surface layer. The most commonly found functional groups are carboxyl, hydroxyl, ketonic, cyclic acid anhydride, ester, hydrocarbons and some nitrogen containing groups, the primary atoms being Oxygen Hydrogen and Nitrogen [7, 35].

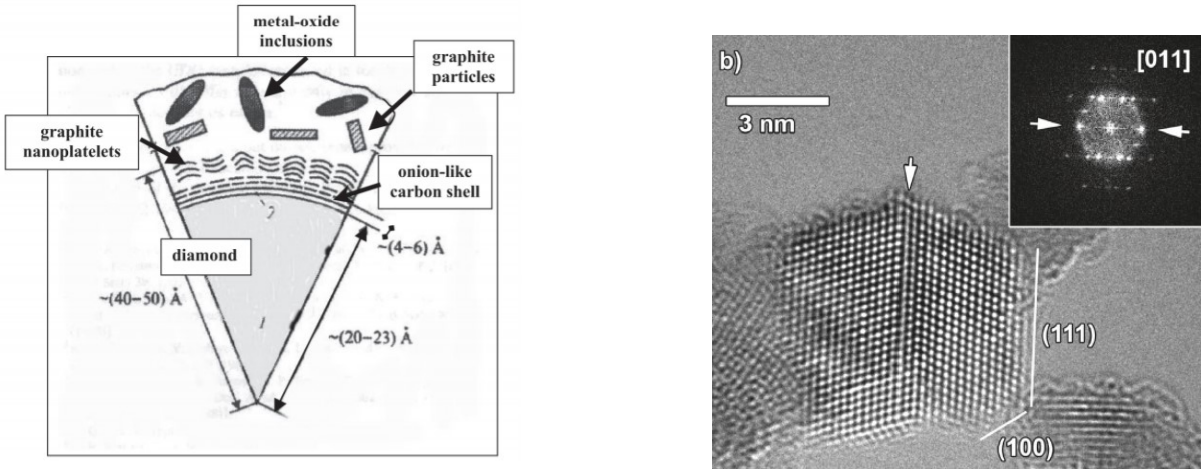

Figure 2: *(left)Model of non-purified nanodiamond particle obtained from explosive detonation synthesis [23], (right) A high-resolution transmission electron microscope image of a ~6-nm detonation nanodiamond (ND) particle, demonstrating crystallographic structure of the nanodiamond core [11].*

3.2 Detonation synthesis

DNDs were first synthesized by the decomposition of high-explosive mixtures in a negative oxygen balanced environment. The negative oxygen balance is required if z<x (Equation 1) because the oxygen provided by the molecule is not sufficient to oxidize the entire carbon. The most common explosive used is Composition B, which is a mixture of TNT and hexogen in the ratio 60:40 (*hexolite*) or 70:30. Other explosives like TNT/RDX and precursors like carbon black or graphite, are also used. A combination of different explosives, and the fraction of diamond recovered from the detonation soot as a function of the composition of the different explosives is provided in (see Figure 3). A closed metallic chamber is filled with inert gas, for example, N_2 or CO_2 (dry synthesis), or water/ice (wet synthesis) coolant, and the explosive is detonated inside (see Figure 4). Detonation soot that contains DND is the resultant of the detonation process. Depending on reaction conditions, the detonation soot can contain 60-80wt% of nanodiamond particles, with the remaining soot consisting of hybridized carbon and other incombustible impurities [1,34, 35]. The reaction goes as follows:

$$C_xH_yO_zN_w \rightarrow a\ CO_2 + b\ CO + 0.5wN_2 + c\ H_2O + + d\ H_2 + e\ O_2 + f \quad (1)$$

Methane, ammonia and nitic oxides are also formed depending on the detonation conditions. The resultant substances contain the following equilibria.

$$CO_2 + H_2O \rightarrow CO + H_2O \text{ (Water gas equilibrium)} \quad (2)$$

$$CO_2 + C \rightarrow 2CO \text{ (Boudouard equilibrium)} \quad (3)$$

$$2H_2O \rightarrow 2H_2 + O_2 \text{ (Dissociation of water)} \quad (4)$$

In this synthesis method, the explosive materials serve as both source of carbon, and energy, owing to the soot forming properties of TNT and high energy containing hexogen. Within the first 10^{-6} s a pressure of 20-30GPa and a temperature of >2000K is achieved by the explosive shock wave [1, 34].

3.2.1 Mechanism of formation of DND

Initially, the shock wave created by the explosive detonation compresses the explosive material inside the chamber and heats it to the point of decomposition, which results in the release of enormous amounts of energy. All of this happens in less than 10^{-6} s. The following steps take place inside the detonation chamber [7, 34, 37]

1. Decomposition of the explosive molecules (~1ns) after which primary carbon cluster of the range <2nm in size are formed.
2. Along the isentropic line (represented by the red line in Figure 4) the carbon clusters coalesce into carbon droplets of size >2nm. The duration of this process is around 10^2-10^3 ns, at pressure 16.5GPa.
3. These liquid carbon droplets crystallize along the isentropic line, in the region between 9-16.5GPa and the duration is $>10^3$ ns.
4. The growth of the diamond stops when the pressure drops below 9GPa, which is represented by the diamond-graphite equilibrium line.
5. After this stage, graphite formation replaces the diamond growth.

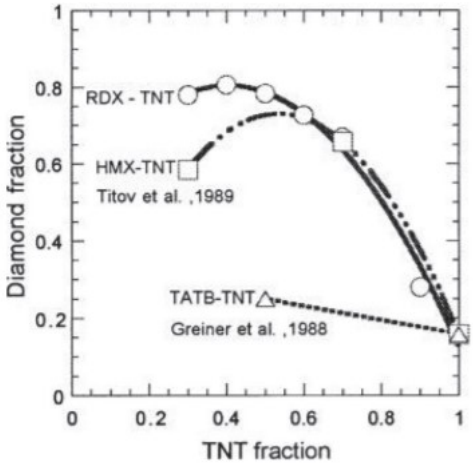

Figure 3: *Fraction of weight of diamond recovered from soot as a function of composition of explosive mixture (TNT – 2-methyl-1,3,5-trinitrotouluene, HMX – octahydro-1,3,5,7-tetranitro-1,3,5,7-tetrazocine, TATB – 2,4,6-trinitro-1,3,5-benzenetriamine, RDX – hexahydro-1,3,5-trinitro-1,3,5-triazine) [7].*

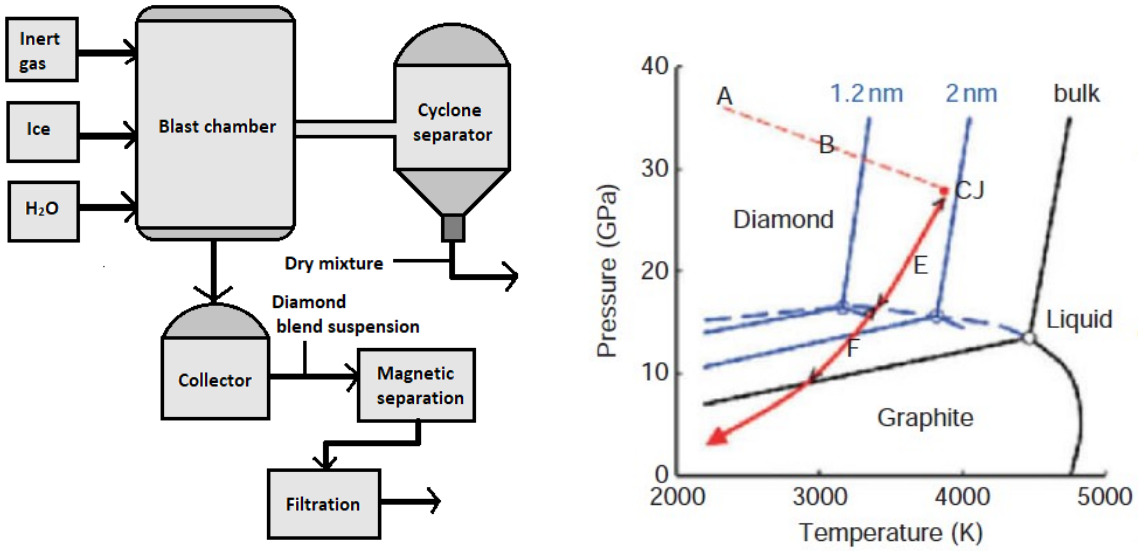

Figure 4: *(left) Flow chart – detonation synthesis of nanodiamonds, modified from [34], (right)Phase diagram representing bulk and nanoscale carbon [37].*

The above phase diagram (see Figure 4) is a representation of both bulk carbon (black lines) and carbon at nanoscale (blue lines). In addition to pressure and temperature as parameters, the cluster size is also taken into consideration. This is because at nanoscale the surface energy considerably affects the Gibbs free energy causing the stable region for DND to shift to higher pressure, and liquid carbon region to lower temperature. Point A represents the front of the detonation shock wave. The CJ (Chapman-Jouguet) point corresponds to the condition of completion of energy release and reaction. In the nanoscale-carbon phase diagram, the CJ point of several explosives lies in the region of liquid carbon, as calculated by two different research groups [1, 7]. The red line indicates the trajectory of the pressure-temperature during the

formation of detonation nanodiamonds. The pressure and temperature at the CJ point are not enough to produce bulk liquid carbon but are sufficient for liquid carbon production at nanoscale. From this, it can be inferred that ND is formed by homogeneous nucleation in the volume of the supersaturated carbon vapor through condensation and crystallization of liquid carbon [7].

The resultant product of the explosion, called the detonation soot, is a mixture of diamond particles (between 2-10 nm in size) [7, 37, 32, 43], various carbon allotropes and metallic impurities. The diamond phase varies between 60-80wt% depending on detonation conditions. The carbon yield is 4-10% weight of the explosive charge and it depends on the cooling media. The incombustible impurities (metal and oxides) contribute 1-8wt% [37, 49, 50].

3.3 Post synthesis purification of DND

The major steps involved in the production of DND are the detonation synthesis followed by chemical treatment, acid removal and product conditioning. Since the detonation soot consists of various impurities (see Table 2) that originate from the walls of the detonation chamber, purification of the resultant soot is required to obtain pristine nanodiamond particles [1, 34].

Table 2: *Contents of combustible impurities according to atomic emission spectroscopy data (*Produced at RFNC-ARITP (Russian Federation Nuclear Centre - All-Russian Research Institute of Technical Physics) [32].*

Impurity	**Typical ND* (mass %)**
Fi	0.1
Cr	0.5
Xi	0.15
Al	0.01
Na	0.05
K	0.002
Cu	0.003
Ca	0.01
Mg	0.005
Mn	0.001
Ti	0.002
Pb	0.001
Total	0.84
Incombustible residue (%)	1.4

Purification also removes the sp^2- hybridized carbon along with impurities from the detonation soot, for which strong oxidizing agents are used. This is because sp^2- hybridized carbon is easily oxidized compared to sp^3-hybridized carbon [48]. Various liquid oxidants used include HNO_3, HNO_3/H_2O_2, $K_2Cr_2O_7$ in H_2SO_4 and KOH/KNO_3 [51]. One purification method that is reported often involves the use of nitric acid (60% concentration) and desalted water at elevated

temperatures and pressures. The process is divided into preparation, treatment and post-treatment steps [37, 51].

Preparation: The preliminary mixture of detonation soot is prepared by removing debris using sieving, magnetic separation and drying. The aqueous nitric acid solutions, where both fresh concentrated acid and recycled acid (recycled post-treatment) is prepared. The moving homogeneous detonation soot suspensions in aqueous nitric acid solution is prepared by mixing the detonation soot and acid solutions [51].

Treatment: The suspension is subjected to continuous thermal oxidation in pressure vessels. Special equipment is required for this step. Tandem flow-through vessels operating at around 500K and 8-10 MPa are used. Primary oxidation of carbon takes place at atmospheric pressure, releasing nitric oxide andCO_2. Oxidation of sp^2-hybridized carbon takes place at elevated temperatures, around 220-260°C. The thermal oxidative treatment products are then separated, and the ND suspension is removed from acid and other impurities by sedimentation [51].

Post-treatment: Nitric acid solution is recycled. This step involves the re-oxidation of nitric oxides by air oxygen, and up to 75% of initial nitric acid can be returned. The acids are removed from ND by flushing, which is done at temperatures up to 80°C. If acidic NDs are present, they are neutralized using aqueous ammonia. The alkali solutions, acids vapor and other waste products are purified based on waste content. Stabilized and normalized NDs are suspended in distilled water. Final DND suspensions in aqueous or water-organic medium are produced, based on set standards. DNDs dried for the preparation of homogenous ND powder. The most popular commercial product is the powder form of DND, even though they have a higher chance of aggregation, due to the ease of transportation and storage [51].

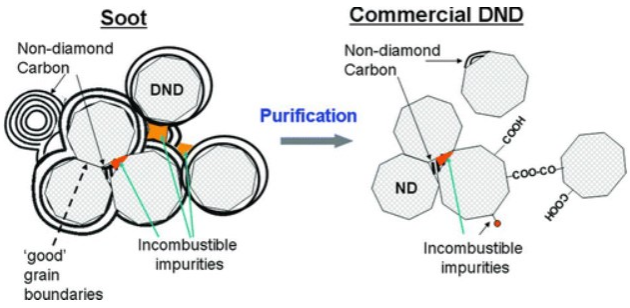

Figure 5: *Purification of detonation soot leading to production of commercial DND [14].*

The purification methods directly affect the average size, surface functionalization and amount of incombustible impurities present in the final product and a suitable method is chosen based on the application for which the DNDs are required [37]. Elemental composition of commercially produced and laboratory produced DND are presented in Table 3.

Table 3: *Elemental composition of Commercial DND samples. A - purchased from Federal Science-Production Centre "ALTAI", Biisk, Siberia, Russia B, B' – purchased from Gansu Lingyun Nano-Material Co., Ltd., Lanzhou, China [49].*

Sample	C (%)	H (%)	N (%)	O (%)	Ash (%)
A	83.94	0.94	2.18	10.50	2.38
B	85.63	1.77	2.12	9.01	1.47
B'	89.84	1.01	2.20	5.76	1.19

For present day applications, especially biomedical applications, it is required that extremely pure DNDs are manufactured. Additional purification steps, including treatment with HCl, HCl/HNO_3, HF/HCl and H_2O_2-NaOH are shown to bring down the incombustible substance content down to 0.5%wt. Of these, treatment with HF followed by HCl achieved the most efficient removal [7, 44]. Heat treatment in air between 44-600°C has shown to improve stability of DND dispersions in water. Significant removal of sp^2 carbon was achieved using Cl_2 treatment at 850°C along with removal of impurities like Al, Cr, Si and Fe [7]. Elemental composition of commercially available DNDs are presented in Table 3. DNDs purchased from Carbodeon used in the experimental section contain <1.2wt% of incombustible impurities.

Table 4: *Elemental composition and purity of ND isolated by nitric-acid purification from DB prepared using different types of reducing agents [32].*

Reducing agent	Explosive: reducing agent (mass: mass)	Elemental composition of ND (mass%)				Incombustible impurities content (mass%)	ND purity (mass%)
		C	H	N	O		
Hydrazine hydrate	1:0.1 1:0.5 1:2.0	93.6 94.4 95.2	1.2 0.4 0.7	2.3 2.5 2.3	1.7 2.3 1.6	1.2 0.4 0.2	97.8 98.5 98.8
Urotropin	1:0.25 1:0.5 1:1	94.9 95.2 96.0	1.1 1.0 0.4	2.5 2.2 2.6	1.4 1.5 0.7	0.1 0.1 0.3	99.1 98.9 98.8
Urea	1:0.5	94.3	1.6	2.7	0.8	0.6	98.0
Ammonia	1:0.5	92.7	2.4	2.9	1.3	0.7	98.4
No additive	-	88.5	1.1	2.2	8.2	-	-

3.4 Surface functionalization

The surface of the purified DND contains a plethora of surface groups that include carboxylic acids, esters, ethers, lactones, ketones, anhydride, amine, nitro, alcohol, alkene, lactone and amide [7, 52]. Apart from the abovementioned purification method, DNDs are surface modified by various treatments to obtain further purified DNDs with small size and reduced agglomeration. In addition, surface modification helps alter the surface chemistry of DND surfaces, thus enabling DNDs to be used in a wider range of applications. Surface functional groups help in maintaining the face reconstruction thus preventing graphitization of sp^3 carbon [48]. The resultant DND is expected to have average particle size close to primary particle size (2-10 nm), high stability suspension with minimum agglomeration, low sp^2 content, low to almost no impurities, and homogenous surface functional groups [1, 26, 48].

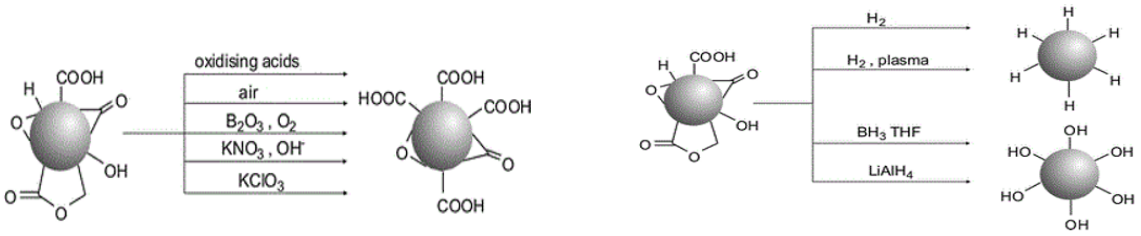

Figure 6: *Oxidation and reduction treatments to produce homogenous nanodiamond surfaces [52]*

In the industrial purification method, the use of oxidizing acids removes amorphous sp^2 carbon and graphitic carbon, and metallic impurities. Surface functional groups, mostly carboxylic groups are attached to the DND surface [16]. Figure 6 shows oxidation and reduction treatments that can be used to homogenize the DND surface. They include gas treatment, (air, H_2, O_2), wet chemistry (KNO_3, $KClO_3$, $LiAlH_4$, HNO_3, H_2SO_4) and oxygen plasma treatment (Air, Fluorination, O_2) [14, 52].

The different oxidation methods include catalytic oxidation (O_2 + catalyst, 420 °C), ozone oxidation (O_3 ; 20 °C), chromic oxidation (CrO_3 in H_2SO_4 medium; 100 °C), perchloric acid oxidation ($HClO_4$, 100 °C), nitric acid oxidation (HNO_3 in H_2O, 100 °C), oxidation by a mixture of sulfuric and nitric acids (HNO_3 in H_2SO_4, 200-250 °C), hydrogen peroxide oxidation(HNO_3 + H_2O_2 in H_2O) [26]. Wet chemical oxidation is the most commonly used because of the wide range of surface functionalization possible. Additionally, they do not require elevated temperatures like gas treatment. However, gas treatment does not require the use of toxic chemicals and catalysts [26, 44]. Chromic anhydride or chromate solutions in sulphuric acid are the most commonly used liquid oxidants because the purification can be done at 120-150°C at atmospheric pressure. O_2 and air are the widely used gas oxidants. Oxidation temperature is a significant parameter because of the risk of oxidation of diamond yield. Oxidation temperature of 425°C is shown to increase sp^3 carbon by the removal of sp^2 graphitic and amorphous carbon. But a temperature above 760°C causes complete oxidation of DND [10]. The oxidation of detonation soot using ozone at elevated temperatures has been

realized at industrial scale and it is very efficient in removing sp^2 carbon, along with being environmentally friendly compared to the liquid oxidant method which uses corrosive oxidants. [7]

In reduction processes, Krueger et al. used borane or lithium aluminium hydride to reduce DND, eliminating oxygen containing surface groups and replacing them with OH surface groups. They further attached alkyl silanes to the DND surface and the product was used in biomolecule attachment [54]. They reported the significant reduction in size of aggregates with the use of borane for DND reduction along with ultrasonication. Hens et al. used lithium aluminium hydride to form aminated DNDs [55].

Fluorination of DND with atmospheric plasma treatment has been shown to remove surface functional groups like -OH and C=O (depending on initial DND type) subsequently forming C-F bonding like CF, CF3(CF2) and C=CF2. This treatment has shown to reduce average agglomerate size by ~20% [14]. Additionally, NDs can be surface graphitization created by annealing of NDs in vacuum, where powerful C–C bonds are created between the graphitic shell and the surface functional groups on the ND [48].

4 Agglomeration in DND

Commercially available DND particles with primary particle size between 2-10 nm are found to exist in loosely bound aggregates at normal pressure and temperature [37]. When DNDs are formed in the explosion chamber (Chapter 2) they are formed as nanodiamond crystallites of range 2-10 nm most of which are found to be in the range of 4-6 nm. Following initial crystallization, the NDs along with the detonation products are continually subjected to turbulent environment. This results in collision of the crystallites with each other as well as with walls of the chamber leading to tightly aggregated particles of size range of few tens of nm [56, 57]. The purification process (Chapter 2) results in further agglomeration, causing the resultant DNDs to be aggregates of a few 100 nm. Further, agglomeration is affected by factors like electrostatic interactions and covalent bonding between nanodiamond particles, interaction with dispersion medium, relative stabilities in dispersion medium and shape of the particles [56]. Larger agglomeration can be broken using ultrasonication. But the primary aggregates are almost unbreakable using traditional ultrasonic techniques, and require methods like bead milling, centrifugation, fractionation and bead assisted sonic integration [26, 49, 58].

Table 5: *DND particle aggregation classification [49].*

Equilibria in suspension	**Average diameter (nm)**
Primary particle	2-6
Agglutinate	ca.60
Core aggregate	100-200
Immediate aggregate	2000-3000
Aggregate powder	20000-30000

4.1 Mechanism of agglomeration

The initial aggregation of the NDs into tightly formed aggregates (few tens of nm) are called *agglutinates* and the randomly arranged aggregates due to physical interaction (100 nm – 3 μm) are called *agglomerates.* There are two theories the try to explain the mechanism of agglomeration of detonation nanodiamond particles [66].

The first mechanism of agglomeration has been explained by A. E. Aleksenskii et al. [34, 56]. It is stated that the initial agglutination is caused by

- the formation of electric double layer around the DND particle (see Figure 7a).
- the bridging of particles in the presence of metal ion impurities. The shells are chemically anchored by the C-C bonds as well as the coupling of -COOH groups by metal ions (see Figure 7b).

They conclude that for fractal diamond agglomerate, there are two types of bonds. The primary DND agglutinates are a result of chemical bonding as explained above. The secondary agglomerates are formed due to the van der Walls forces [56].

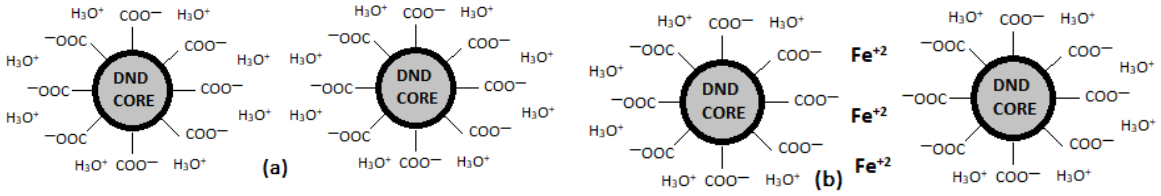

Figure 7: *(a) Electric double layer formation around a DND particle in dissociation of carboxyl groups, and (b) Formation of bridge bonding in the presence of iron ions, initiating DND particle coagulation [34].*

A more recent discovery by A. Bernard suggests that the individual particles exhibit anisotropic facet-dependent variations in surface electric potential. (100) facets had positive charge and (111) facets had either negative or neutral charge. Two thermodynamically favourable configurations namely, positive $(100)^{+}$ with near-neutral $(111)^{0}$, and negative$(100)^{-}$ with near-neutral $(111)^{0}$ were found to be preferred. These interactions are called Coherent Interfacial Coulombic Interactions (CICI). Other random electrostatic interactions are called Incoherent Interfacial Coulombic Interactions (IICI). There interactions are significantly different from van der Waals interactions, that form loose aggregates [58].

The agglomeration can be broken down by mechanical deagglomeration methods and surface modification methods (Chapter 3.4).

Table 6: *DND aggregate interfacial coulombic interaction comparison. CICI - Coherent interfacial coulombic interaction IICI - Incoherent interfacial coulombic interaction vdWA - Van der Waals aggregation [58]*.

Name	Size (nm)	Nature	Configuration	Terminology
Agglutinate	ca.60	Electrostatic	Ordered	CICI
Agglomerate	100-200	Electrostatic	Random	IICI
Aggregate powder	>1000	Van der Waals	Random	vdWA

4.2 Mechanical deagglomeration

The goal of deagglomeration is to obtain high stability DND suspensions with primary particle size between 2-10 nm. The post synthesis processes including purification and surface modification assisted deagglomeration, but the aggregate size (>200 nm) is far from the primary particle size. For many biological applications, it is required that the nanodiamond aggregates are as small as possible, to aid in the interaction with the biological molecules. Mechanical deagglomeration methods are used to obtain DND suspensions with particle size approximating the single digit core particle. These methods are used on commercially purchased DNDs which are found to have strong agglomeration. The most commonly used mechanical deagglomeration methods are discussed below [26, 37, 56].

4.2.1 Centrifugation

A centrifuge carrying the DND suspension that rotates around a central axis at high speeds is used in this method. As the centrifuge rotates, particles with relatively higher densities are flung to the outer section away from the centre, with the densest particles on the outermost section. The deagglomeration is possible by the water pressure created during centrifugation. This causes the penetration of water into the nanogaps/nanopores in the agglomerates, thus breaking them. Suspensions with particle size below 20 nm are obtained by fractionation, provided the acceleration is above 3000g [7, 37].

This method is free from contamination, but colloidal stability is very important. It is almost impossible to fractionate an unstable suspension. The shape of aggregates obtained by this method are found to be irregular, with spherical and elongated chains. But the contents of surface groups on each individual particle is more uniform compared to other methods like bead milling. DND separation based on different agglomerate sizes is possible with this method. This is useful when specific sized agglomerates are required. For example, size range below 10 nm are preferred for biomedical application, size range 50-100 nm are preferred for UV protection coatings and polymer composite fabrication, and size range 150-200 nm are used to form photonic structures that cause diffraction in the visible region [37].

4.2.2 Bead milling

The bead-assisted milling or stirred media milling method uses micron-sized ceramic or zirconium beads in a stirred mill. The beads are agitated to cause high energy impact and shear force on the agglomerates, in turn breaking them. The disintegration to primary particles is caused by the collision of beads and the centrifugal force. Head-on collision, shearing collision, and collision to the inner wall of the nanopore take place, breaking up to 90% of core aggregates. Bead milling also assists in dispersion of the powder in the solution [31, 37].

Formation of additional graphitization could be a problem in bead milling. The zirconium beads (30µ diameter) cause heavy impact on a small contact area causing the formation of high temperature and pressure, converting diamond atoms on the surface into sp^2 hybridization leading to diamond-graphite transition. Additional purification step maybe required to remove the sp^2 carbon contamination. Further contamination is caused by the zirconium particles (5nm diameter) from the micro beads. Several methods including liquid oxidizers, NaOH solution and molten NaOH, and strong acids have been used in purification of DND primary particle suspensions from surface graphite layers and metallic impurities [14]. Nevertheless, bead milling is a commercially successful technique to produce DNDs with 'Nanoamando' being a very popular manufacturer of DND used in biomedical research [31].

Figure 8: *Schematic of bead milling method (left) and bead assised sonic integration (right) [60].*

4.2.3 Bead assisted sonic disintegration

Bead assisted sonic disintegration is a combination of ultrasonication and bead milling and was first introduced by Ozawa et al. [59]. They used a 400W sonication bath equipped with a horn-type sonotrode with the DND suspension and additionally Zirconia micro beads were added to the solution. The sonotrode generates high powered shock waves that accelerate the micro beads. By using high power sonotrode, deagglomeration is sped up and abrasion from zirconia and further contamination is reduced. The stability of the solution depends on the polarity and hydrogen bonding ability of the solvent [60].

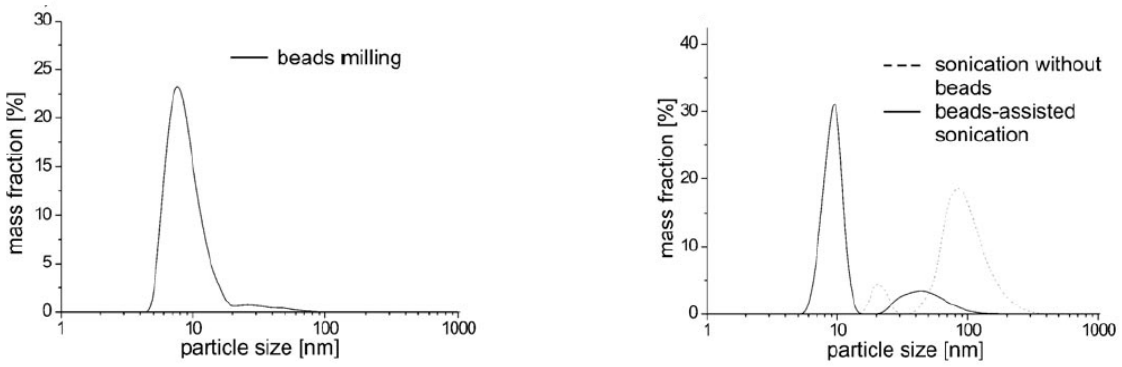

Figure 9: *Comparison of primary DND particle size obtained bead assisted milling (left) and bead assisted sonic milling (right) [60].*

Table 7: *Different mechanical deagglomeration methods [47]*

Method	**Additive**	**Power(W)**	**Workup**	**ND size (nm)**
Centrifugation		500	Centrifugation at 18000g, lower g yields bigger primary particle size	4
Bead milling	ZrO2 microbeads	-	ZrO2 contamination treated with strong acid or base	<10
Bead Assisted Sonic Disintegration	ZrO2/SiO2 microbeads	400-450	ZrO2 contamination treated with strong acid or base	4-5

5 DND Biocompatibility

5.1 Biocompatibility and cytotoxicity studies

The toxicity studies of DND are relatively complicated due to the vast variation in manufacturing, purification, and surface modification of DNDs [61]. The considerable toxic impurities of the material can be removed by appropriate purification methods, but the inherent toxicity of the DNDs are the point of focus in biocompatibility studies [62, 63]. Although materials like glassy carbon and diamond are classified as non-toxic substances, at nanoscale they might not be tolerated by cells. DNDs have small uniform nanoscale particle size that are like many biological compounds. However, they are capable of penetration into cells and might affect the functionality of the cellular respiration through interference in the redox process [3]. Various surface modification procedures are available to selectively purify DNDs and render them suitable for biological applications [37].

Methods of assessment

MTT (3-(4,5-dimethylthiazol-2-yl)-2,5-diphenyltetrazolium bromide) assay is primarily used in evaluating cell health after DND exposure. This method employs spectroscopic studies to monitor the cell viability after exposure to sample particle. Cell viability is tested by the ability of mitochondria to reduce the tetrazolium salt. This changes the colour of salt from yellow to purple evidencing cell life. Other commonly used tests include XTT ((2,3-bis-(2-methoxy-4-nitro-5-sulfophenyl)-2H-tetrazolium-5-carboxanilide) and WST (water-soluble tetrazolium salts) assays, morphological examination, neutral red assay and reactive oxygen species (ROS) production. Inside the cell, toxicity effect is typically characterized by the damage to lysosomal membranes, increased expression of proinflammatory mediators and cytokines (immune response) which causes ROS generation leading to oxidative stress and eventual cell death [37].

In vitro studies:

In vitro studies conducted to evaluate the biocompatibility of DND particles demonstrate high biocompatibility [10, 37, 61, 62]. But some studies also show cytotoxicity at genomic level [61, 62]. Cytotoxicity study by Sc et.al. using MTT and fluorescent(ROS) assays focusing on mitochondrial toxicity evaluation [41, 64] revealed no significant reduction in cell viability (meaning no significant damage to mitochondria) indicating low ND toxicity. Size related studies using micron sized diamond powder [65] and DNDs of size 2-10 nm show slight differences in cell viability with MTT assays, with the former having increased cell viability.

DND surface chemistry impact on biocompatibility has been evaluated by [1,2,40,41]. DNDs containing surface groups -COONa, -COOH and -SO_3Na were found to be nontoxic when evaluated using MTT assay on various cell lines [62]. In terms of genomic studies, acid purified DNDs' effect on cytokine expression showed no significant change in the expression [51]. Functionalization of DNDs with biomolecules evaluated with rodent ovary cells showed no cytotoxic effects [69]. However, some studies have shown oxidized DNDs to alter the expressions of DNA proteins in embryonic stem cells [70] and human airway epithelial cells [71]. But in comparison to MWCNTs used in the same experiments, NDs were found to have much lower levels if change and relatively increased biocompatibility [37].

In vivo studies:

DND biocompatibility studies *in vivo* are slightly more complex due to the low colloidal stability and high polydispersity [72]. Micro and nano-sized ND implants on canine knee joints [73] did not contribute to inflammatory response. However, a study [74] shows that DNDs injected into the muscle can pass the blood-brain barrier in mice. Although further investigation of the long-term pathological effects of internalized NDs on the cells is an ongoing study, the current toxicity tests suggest NDs as potential biocompatible materials [33, 35, 37].

Comparison with other carbon nanoparticles:

Studies by Jia et al. concur with recent studies [75, 76] in suggesting that factors like mass, purity and aspect ratio, directly affect the biocompatibility of nanodiamonds. When tested with guinea pig alveolar microphages biocompatibility was established in the order of NDs>C_{60} > 99.9%>SWNTs (>95%) & MWNTs (>90%). [77] Studies on neuroblastoma (neuronal line) and alveolar macrophage (lung cell line) in aqueous suspensions of NDs in relation to CB, MWNTs and SWNT, found that NDs were more biocompatible with no significant disruption to mitochondrial membrane and absence of ROS [77]. The trend for biocompatibility was found to be ND>CB>MWCNT>SWCNT. NDs have been consistent in showing better biocompatibility results in comparison to similar sized carbon nanoparticles [7, 20, 37, 62].

Long term biocompatibility:

DND biocompatibility depends on various factors including particle size, exposure time, cell-specific responses, concentration, synthesis and purification methods, functionalization and further alterations. Current researches agree on biocompatibility of DNDs with mammalian cells [37, 62, 65]. However, to understand the long-term toxicity effects of DNDs, factors like dosage, administration routes, effect of individual particles and clearance need to be addressed. DNDs, being relatively new candidates for biomedical applications, are not yet established as completely safe and non-toxic for *in vivo* applications.

5.2 DND thin films - biomedical applications

The unique size range of DND particles, ~2-6 nm, falls under the size scale that includes many bio-compounds. DNDs can be tailored for different biological environments in the form of particulates, coatings, and thin films substrates. Their large surface area, 330 – 400 m^2/g vastly improves the adsorption capacity for binding biomolecules to the DND surface. [1, 37] The specific gravity of DNDs is 3.5 $g/cm^{2,}$ which provides solid phase support when dense structures are fabricated. Binding capacity of DNDs to similar sized molecules is high, for example 10 times greater than nanosilica, helps in physisorption of proteins and other small molecules like afflotoxins [20].

During the purification and modification stages of DND production, oxygen containing surface functional groups are introduced, making the surface relatively hydrophilic and improving the adsorption of biomolecules *in vivo*. DND surfaces can be further functionalized through chemical, photochemical, mechanical, enzymatic and laser assisted methods. which opportune the attachment/adhesion of various biomolecules [37]. Some of the biomedical applications of DND thin films are discussed in the next section.

5.2.1 DNA immobilization for the fabrication of biologically active ND thin film substrates

Wensha et al. fabricated DNA-modified thin-films on DND thin films coated on silicon and gold substrates. C-H terminated DND thin film on Silicon substrates were created with UNCD powder. Thiol-modified DNA was used to produce the DNA modified thin film substrates, where the DNA molecules are covalently immobilized on diamond. The stability of the thin films was examined using fluorescence intensity tests [8]. Figure 10 shows variations in fluorescence intensities over 30 successive cycles of hybridization and denaturation and the UNDC thin films show no measurable decrease in signal intensity even after 30 cycles, exhibiting extremely good stability and selectivity.

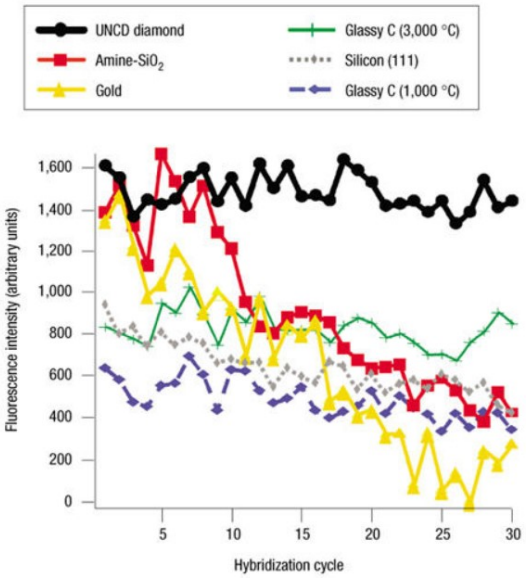

Figure 10*: Variations in fluorescence intensities over 30 successive cycles of hybridization and denaturation [8].*

Apart from DNA immobilization, DND thin films are also used to immobilize proteins on the surface of the biosensor [9]. Such biosensors are used to detect various interactions like protein–nucleic-acid, antibody–antigen, protein–lipid, protein–small-molecule interactions and protein–protein interactions [13, 78].

5.2.2 Biosensor for the electrochemical detection of neurotransmitters using ND electrodes:

Currently available neurotransmitter detection methods like spectroscopic methods and micro-dialysis, although selective and safe, are incapable of providing real time measurement signals. This is especially important in case of neurotransmitter detection, because the transmission events between the synapses take place in sub-second range. This calls for a measurement technique that can provide acute temporal resolution, along with sufficient selectivity and sensitivity. [13, 31, 79]

Electrochemical detection of neurotransmitters could be a desirable method for real time measurement with acute temporal resolution for electrochemically active neurotransmitters such as dopamine, meaning that they undergo redox reactions with a target molecule and the detection of electrons involved in the reaction gives accurate reading on the concentration [79-81].

There are several challenges in designing an appropriate biosensor for the detection of Dopamine. The concentration of dopamine in the extracellular fluid is very low ($0.01 - 1\ \mu M$), demanding an extremely sensitive sensor [31]. The extracellular fluid contains numerous electrochemically active compounds belonging to the second and third categories of neurotransmitters mentioned. The biosensor design needs to be selective to the compound of interest. Biocompatibility, miniaturization, and functionality are other important factors to take into consideration in sensor design [50, 81].

In electrochemical biosensors, the electrode material plays an important role in influencing the reaction kinetics of the reacting species. Carbon based electrodes possess a wide potential window for the redox reactions, proving suitable for such biosensors [10]. Studies [28, 29-31] have shown NDs to be excellent materials to probe electrochemical activities. The structure of NDs demand high surface to volume ratio, thus rendering the surface properties dominant. The oxygen containing surface groups and conductive sp^2 shells around the NDs might possibly improve their electrochemical activity. A detailed research of NDs as suitable material for electrodes is provided in the thesis by Elli Leppänen [31]. ta-C + DND hybrid annealed electrodes were electrochemically characterized for dopamine detection. It was found that the sensitivity and kinetics towards dopamine detection were improved compared to non-annealed electrodes [31].

5.2.3 DNDs as electrochemical sensors

Apart from neurotransmitter detection, NDs can also be considered as potential candidates in the electrochemical detection of glucose, uric acid, and sulfa drugs [82]. Nucleic acids are also electroactive species, that can be electrochemically detected [83] and boron doped diamond electrodes, being highly conductive, have facilitated the electrochemical detection of double stranded DNA in aqueous solutions using amperometric methods. [82].

5.2.4 Immobilization of antibodies and bacterial binding on nanodiamond – biosensing:
Antibodies have been widely used in the detection of biological agents including bacteria. Nanomaterials have been researched as potential candidates for fabricating biosensor surfaces for the immobilization of antibodies. [12, 27] Huang et al. [12] studied the immobilization of anti-Salmonella and anti-Staphylococcus aureus antibodies on NDs and CNTs. The NDs were grown on Silicon substrates and were treated with both air and hydrogen plasmas followed by antibody immobilization. Air plasma treatment rendered the surface of the NDs hydrophilic with O, OH, thus promoting interactions between hydrophilic antibody solution and hydrophilic nanodiamond surface. Further investigations into the interaction mechanisms between ND surface and antibodies is required, but NDs have shown promising results as potential candidates for such biosensor surface materials [12, 27].

6 Thin film coatings

As outlined previously, continuous development of modern surface science, biomaterial science and engineering has led to the development of new biomaterials and modification of existing biomaterials based on target applications. Besides bulk properties, surface properties of biomaterials are considered to be important in designing the materials for biosensors. Thin films and coatings are vastly becoming effective techniques for the surface modification and engineering of biomaterials. They are favoured because of the ability to modify them to interact with external systems in specific ways. The ever-decreasing sizes of biomedical devices, which increases the surface area to volume ratio, have also propelled the need for thin films and coatings [20, 54].

The properties of thin films like chemical functionality, solubility, topography and mechanical properties play an important role in the overall functionality of the biosensor. Controlling such parameters is important to optimize the performance and safety of the devices. In biomedical applications, such parameters affect both short-term and long-term functionalities. For example, it is desirable to produce controllable and densely packed nanostructures as thin films along with increased density of functional groups, that enable large number of reaction sites for target analytes [20].

Detonation Nanodimond thin films are produced using sol-gel technique and electrophoretic deposition. DND is used as seeds to fabricate UNDC thin films using CVD and PVCVD methods. A brief introduction of each method is given in the following section. A comparison table consisting of different deposition parameters is presented in Table 8.

Electrophoretic deposition (EPD): It is a wet electrolytic deposition technology employing electrophoresis to fabricate uniform thin films. It is suitable for surfaces with complex shapes and surface morphologies. EPD can be used to fabricate thin films of various thicknesses ranging from nanoscale to microscale, with precise thickness control. In EPD, electric field is applied between two electrodes and charged particles dispersed in the liquid medium move toward oppositely charged electrodes and deposit on the surface of the electrodes, forming thin film coatings [17]. L. Stehlik et al. fabricated dense DND thin films on pyrolytic graphite (HOPG) substrates using electrophoretic deposition. H-DNDs with positive zeta potential and O-DNDs with negative zeta potential deposited on substrates with opposite charges [28, 54]. Major drawback of this method is the poor adhesion with different substrates with different thermal expansion coefficients, especially in biomedical applications. Agglomeration causes uneven coating and deagglomeration process is recommended to precede electrophoretic deposition [20].

Sol-gel technique: In the sol-gel technique, the coating material is prepared in liquid form as a precursor solution. The solution is then deposited on the substrate and heat treatment is used for solvent evaporation and densification. Commonly used sol-gel techniques include spin-coating, dip-coating, drop-casting and spray deposition [20].

CVD: In this technique, DNDs are used as seeds for the production of UNDC thin films. The CVD method uses dissociation and/or chemical reactions of vapour-phase precursors (reaction chemicals) to deposit desired material on substrate surface. An activated environment is provide using thermal energy for the assistance of the chemical reactions and eventual deposition of the thin films [86]. Plasma-enhanced chemical vapour deposition is a method in which, instead of heat source like in CVD, plasma created using radio frequency (RFCVD) or microwave (MPCVD) is used to activate ions and radicals in chemical reactions to form layers on the substrate [23]. To fabricate UNDC thin films from DND seeds, the DND suspensions are ultrasonicated and seeded on Si wafers. The seeded wafers are placed in MWCVD chamber and $CH_4/H_2/CO_2$ precursors are used to grown nanoscale UNCD thin films at 460°C, 3.4 kW power and 0.15mbar pressure [21].

Table 8*: Comparison of different thin film coating methods for fabricating DND thin films [17, 20, 21, 23, 54, 84, 86]*.

Classification	**Deposition parameters**						
	Deposition temperature	**Gaseous treatment**	**Source of energy**	**Materials**	**Deposition thickness range**	**Vacuum require-ment**	**Comments**
Electrophoretic deposition	<100°C	-	DC voltage (25-100V/cm) [88]	functional composite coatings and multilayer films	100nm-80um	-	Thin films with good purity and high thickness control
Sol-gel techniques (Spin coating, Spray coating and Dip coating)	<200°C	-	-	Thin films with aqueous suspensions of nanomaterials and metal salts used as precursors	100nm-2um	-	Good control of chemical composition and microstructure, reduced temperature, homogeneous films, simple instrumentation
Traditional CVD	200°C - 1300°C [88]	Carrier gas Argon, Helium, precursor vapour	Heat energy	Inorganic precursors, silicon-based, metallic films	10nm-3um	10^{-3} – 10^{2} Torr	This method uses DND as seeds to fabricate UNDC thin films
Plasma-enhanced chemical vapour deposition (PECVD) (RFCVD and MPCVD)	50°C - 600°C [88]	Carrier gas Ar, He, precursor vapour	Radio frequency (50kHz - 13.56MHz) Microwave(2.54GHz)	Inorganic precursors, silicon-based, metallic films	10nm-3um	0.1 - 2 Torr	Lower temperature allows temperature sensitive substrates and coatings, used DND as seeds to fabricate UNDC thin films

Sol-gel techniques are simple to use, do not have strict instrumentation and are cost effective, when compared to MPCVD technique. In this thesis, commercial DNDs are fabricated as thin films using spin coating and spray coating methods.

6.1 Spin coating

Spin coating technique is used to create thin film (nm-µm range) coatings on substrates by dropping the solution containing desired coating material onto the substrate, while the substrate is rotating [88]. It involves four steps (see Figure 11) [88]:

1.Deposition: Coating material is dissolved into desired solution, which is the deposited onto the substrate.

2. Spin up: Substrate is accelerated to initial rotation speed and solution wets the surface to form a few micrometres thick coating.

3. Spin off: Spinning speed is increased causing solution to fling off the substrate due to centrifugal rotational forces.

4. Evaporation: The remaining solution spreads over the substrate and starts to evaporate. Only the solvent is removed leaving behind the coating material.

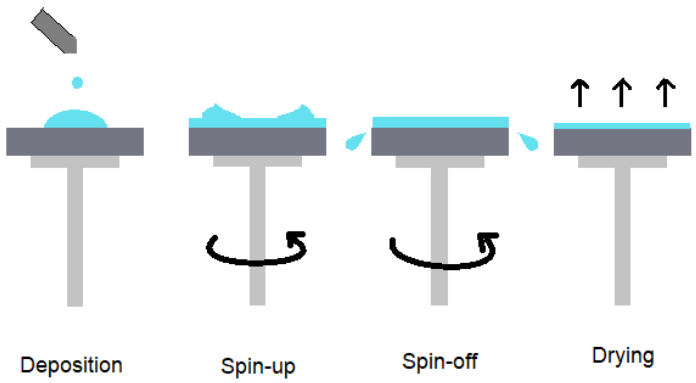

Figure 11: *Schematic representation of four stages of spin coating.*

The centripetal force along with the surface tension of the solution arranges the solution into an even covering and the evaporation leads to even coating material left on the substrate. The parameters that affect the quality of the film coating are initial concentration of solution, choice of solvent material, substrate material and spinning speed. Higher solution concentration and lower rotational speed increase the film thickness [89]. For nanoparticle suspensions, the thin film homogeneity also depends on the aggregation of the particles in the solution.

Spin coating at very low speeds helps in high levels of nanoscale order. The thickness of the film and speed are given by the relation

$$h \propto \omega^{-1/2} \eta^{1/3} c_o \quad (5)$$

where h is the film thickness, η is the viscosity (Pa.s), ω (rpm) is the spinning speed and c_o is the solution concentration (m0 [89, 90].

6.2 Spray coating

Air assisted spray deposition technique is widely used to fabricate thin films due to the low cost and ease of fabrication, and absence of strict instrumentation and toxic waste treatment. There are various spray coating techniques like paper printing by droplet injection, thermal spray coating and spray deposition for thin film fabrication. The simplest and most cost efficient of the above methods is spray deposition [15].

Spray coating occurs through the following steps: liquid atomization, droplet evaporation, impact on the surface, spreading, drying of solvent and adhesion of required coating material [15]. When the solution is atomized, it creates aerosols which are directed on the substrate. The solvent evaporates, and the suspension gets deposited as a thin layer on the substrate [91].

Substrate properties like roughness, droplet spreading, temperature of the substrate and wettability play an important role in the resultant thin film coating. The homogeneity of the thin film coating is affected by spray deposition properties like drop impact dynamics, spray flow rate, nozzle tip size, spray height (distance between nozzle tip and substrate) and solvent properties [15, 88]. The spray height (see Figure 12), can be calculated using the formula

$$H = \frac{C}{2\tan(\phi/2)} \tag{6}$$

Where H is the spray height, C is the spray coverage and ϕ is the spray angle (Figure 12)

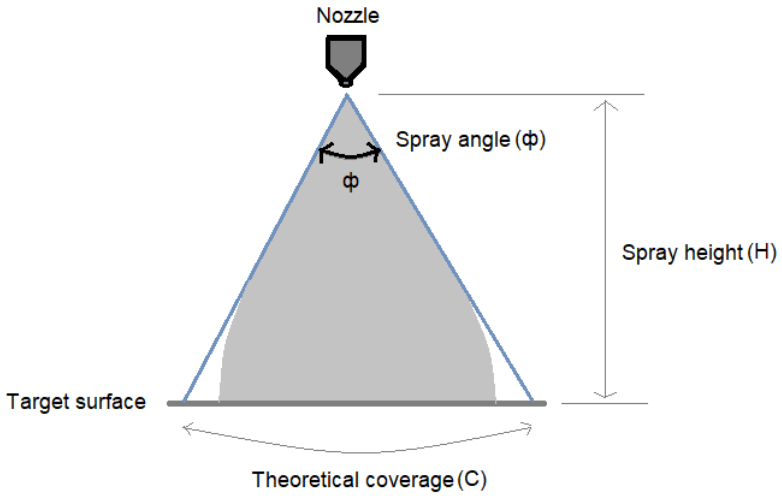

Figure 12: *Representation of spray angle, spraying height and spray coverage.*

In this thesis, the spray coating is improvised by avoiding manual spraying and automating the technique. Using the automated spray coater, several samples are spray coated at the same time, creating the possibility for consistent and repeatable coating results along with ease of fabrication. The spray deposition is combined with movement automation in the automated spray coating device.

6.3 Automated spray coating technique

The device used for the automated spray coating consists of two parts, the moving and the spraying parts. The moving part is constructed using the Prusa i3 3D-printer. Automation is achieved through programming the 3D printer to move in specified paths and directions. The spray deposition is achieved by replacing the extruder of the printer with a spraying unit consisting of nozzle, valves and corresponding electronic circuit. The working setup of the automated spray coating device is shown in Figure 13.

6.3.1 Movement control

The core of the device is an aluminium frame that holds the printer together. There are 3 axes, the x, y and z axes which dictate the movement of the nozzle depending on the input from the user. Stepper motors are present for each axis and are responsible for movement and speed control. The different axes and parts of the device are connected using rods and connectors of different sizes.

A stepper motor is a DC brushless motor moving in discrete steps. It consists of multi-toothed electromagnets arranged around a central gear. An external microcontroller called a driver is used to energize the electromagnets. When the first electromagnet is energized it attracts the nearest teeth of the gear which aligns with it. When the next one is energized, the teeth of the gear align with the energized electromagnet by moving one step. By repeating the process, stepping is achieved. The stepper motor used in this technique is NEMA 17 (42BYGHW811L20P1-X2), bipolar stepper.

The x axis carries the spraying part, which replaces the extruder of the 3D printer, and a stepper motor is connected on the left size of the axis. The stepper motor and the spraying part are connected to a conveyer belt and the movement of the stepper motor correspondingly causes movement of the spraying part along the x-axis

The y axis consists of a base plate on which the samples are placed. A stepper motor is connected at the bottom of the plate and controls the movement and speed of the base plate, through a conveyer belt, similar to x-axis.

The z axis is responsible for controlling the distance between the samples and the tip of the nozzle. It consists of two stepper motors that are coupled to threaded rods. Motor movement controls the movement of the rods, thus adjusting the spraying height.

The base plate of the y-axis is a hotbed, that is used for temperature control during spray coating. The temperature of the hotbed is controlled using the electronics and a thermistor is used to detect the instantaneous temperature of the hotbed. The hotbed is covered with a glass plate, for the protection of hotbed and electronics from spray solutions. The samples to be spray coated are placed on the glass plate.

The three axes frames, base plate and threaded rods are assembled into the final unit as shown in Figure 13.

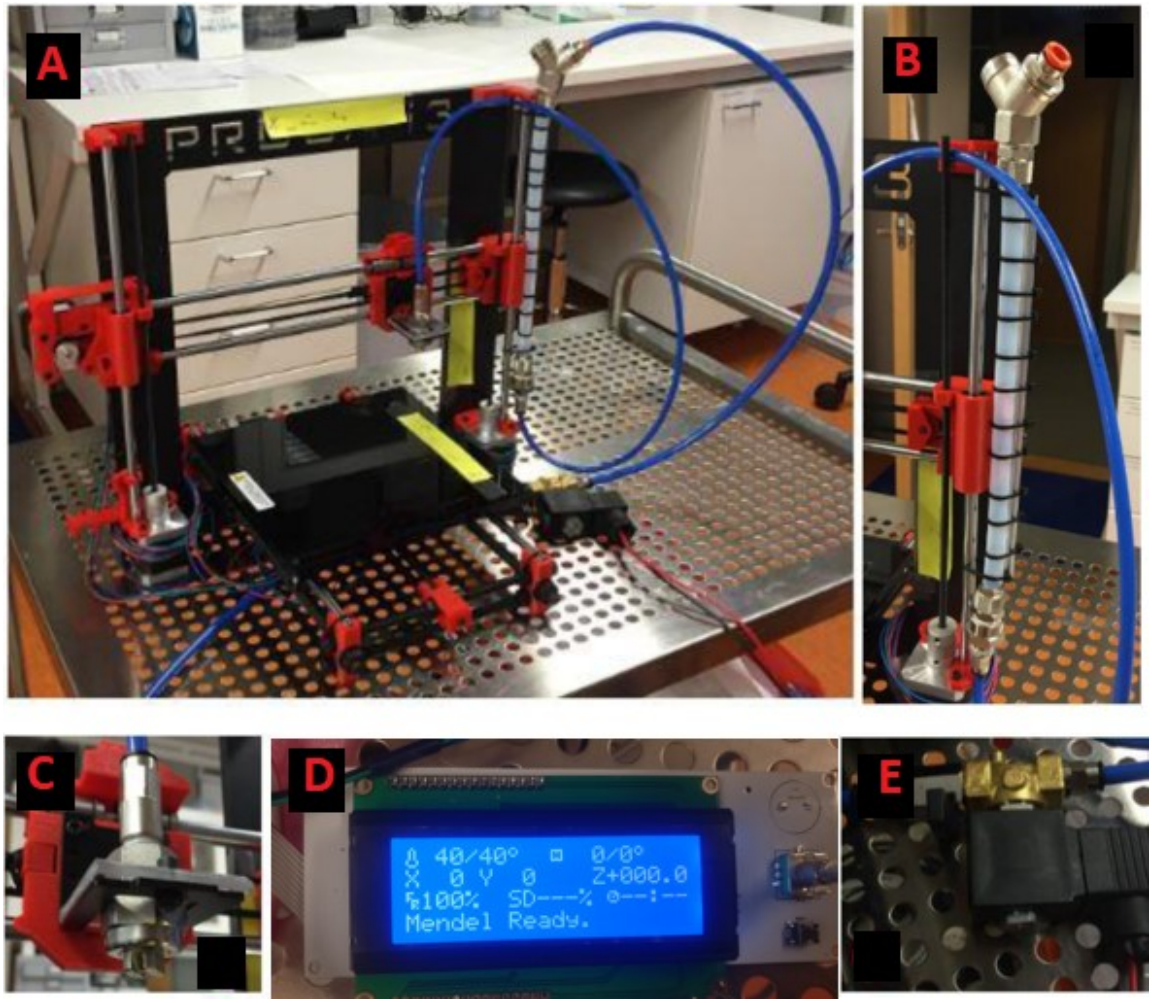

Figure: 13 *A) Assembled movement and spraying part of the device, B) liquid vessel attached to the Z axis of the device, C) Nozzle, D) LCD display, E) Control valves.*

6.3.2 Spray system

The spraying part consists of the spray nozzle, electric valves for nozzle control and pressurized air flow control, ball valve, liquid vessel, air inlet and liquid inlet (see Figure 14

). The air inlet is connected to through the electric valve to the pressurized air source. The liquid inlet is used to fill the liquid vessel with desired spray solution.

A flat fan nozzle (TPU650017-SS) is used, in which the liquid entering the nozzle is fed into a pressure chamber and is ejected through the circular orifice of the nozzle. The nozzle has a flat spray pattern at 65 degrees spray angle and spray flow rate of 133ml/min at 1.5 bars of pressure. The spray height is calculated using the formula from Equation (6). in the experimental part

An electrical valve (12V, 10W) is used for the automatic spray control. Another electrical valve (12V, 10W) is used to control the pressurized air flow to the nozzle, automatically. A

mechanical ball valve is used between the electrical valve and air outlet, in order to avoid air breaks. To store the solution that is required for spraying, a liquid cylindrical vessel of length 20 cm and diameter 1.5 cm made of Polytetrafluoroethylene (PTFE) is used. PTFE is used due to its inertness towards most alcohol-based solutions, so that no particulate material is carried along in the solution and gets deposited on the sample substrate.

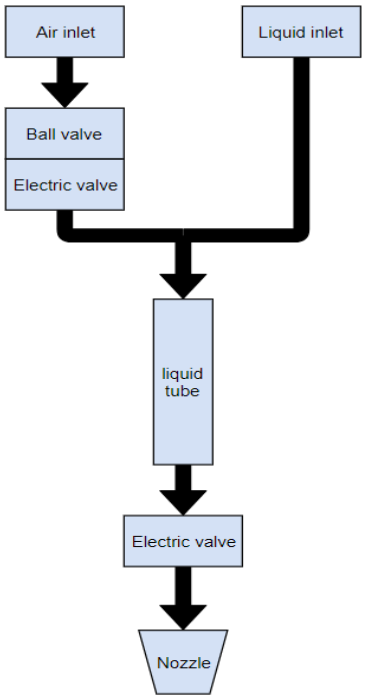

Figure 14: *Schematic representation of the spraying system.*

6.3.3 Electronics and programming

The control unit for the operation of the spraying unit is provided by Arduino 2560 microelectronics board, with RAMPS 1.4 shield (RepRap Arduino Mega Pololu Shield). The Arduino board is controlled using Marlin, which is an open source firmware. The firmware is modified using Arduino IDE software, to allow for the printer to be used as a spray coating device. The electronic circuit connections are shown in the Figure 15. The Liquid Crystal Display (LCD) is used to display the current positions of the x, y and z axes, the set and instantaneous hotbed temperatures. A power supply of 12V, 18A is used to power the electronic circuit, stepper motors and the hotbed.

The following user interface algorithm allows the use of the device as an automated spray coating device.

1. Power supply is switched ON
2. The positions of x, y and z axis are initialized. Current position of each axis is displayed on the LCD.
3. Hotbed temperature is set to desired value. Instantaneous temperature value is displayed on the LCD against the set value.
4. Stepper motor pins are defined.
5. Number of steps are selected as 200 steps per revolution.
6. Speed of the motor is set (between 3000-3600 rpm is the optimal range)
7. The desired spray height is set by switching the Z stepper motors ON for corresponding steps.
8. The spray and pressurized air control electric valves are turned ON
9. For forward movement along x-axis, the required steps are set, and X axis stepper motor is switched ON in the forward direction. To move the x-axis for 9.5 cm, 30000 steps are required.
10. For forward movement along y-axis, the required steps are set, and Y axis stepper motor is switched ON in the forward direction.
11. For reverse movement along any axis, the required number of steps are set, and the motor is moved in the reverse direction.
12. After spray pattern is achieved, the electric valves are turned OFF
13. Steps 7-11 are repeated for desired printing pattern. For example, for one spray along x-axis, the motor is moved along the x axis once in forward direction and control valves are switched OFF.
14. Motor is moved back to initial position.
15. Power supply is switched OFF.

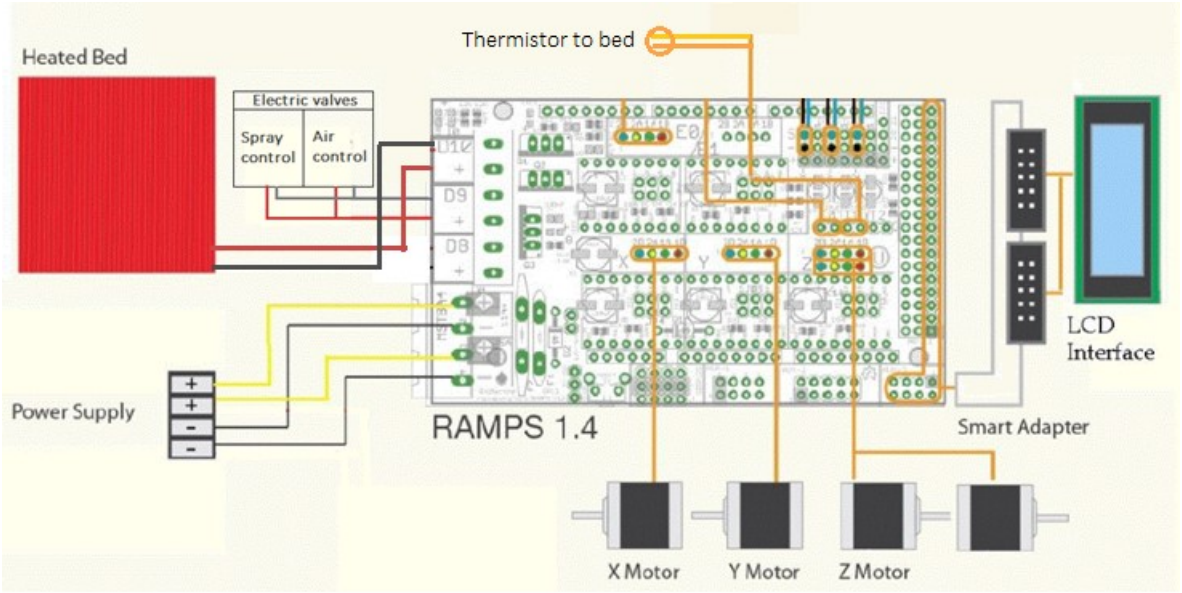

Figure 15: *RAMPS 1.4 electronic circuit with Arduino Mega 2560 board used to control the movement and the spray system.*

7 Scanning Electron Microscopy

7.1 Introduction

Scanning electron microscopes are used when magnification requirements exceed 1000x. In conventional optical microscope, the limiting factor is the wavelength of imaging radiation. This limitation is solved in scanning electron microscopes, where the electrons can be accelerated to energies ranging between 0.1-30keV [92]

In SEM, the area of specimen to be analysed is scanned by irradiation of finely focused accelerated electrons that sweep in raster format. These electrons interact with the specimen sample and produce varying signals including secondary electrons, backscattered electrons, characteristic x-rays, and other photons of various energies. Of these, secondary and backscattered electron signals are the most relevant and useful in image formation. [22, 92]

The different signals arise due to the different interaction possibilities between electrons and the specimen material (see Figure 16), providing us with the flexibility of performing different types of analyses including topology, crystallography, and composition. The main application of SEM is the microstructural analysis of solid objects with the possibility of producing high resolution images with spatial resolution of the order of a few nanometers (1-5 nm). [22]

When a beam of electron enters the specimen, some electrons are deflected into new trajectories due to the dispersed negatively charged atomic electrons. These electrons are 'elastically' scattered with no kinetic energy loss and spread out laterally from the incident beam trajectory. After numerous such deflections these elastically scattered electrons leave the specimen and form the backscattered electron group. The incident electron beam also undergoes inelastic scattering, where the electrons gradually transfer their energy to specimen atoms through different layers until they lose all their energy. This kind of scattering leads to secondary electrons, which are loosely bound conduction band/ outer shell valence electrons, and x-ray signals.

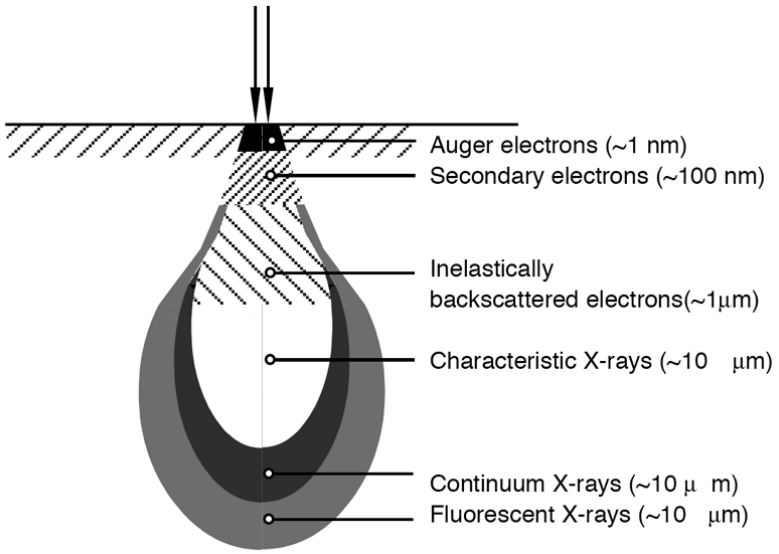

Figure 16: *Interaction volume containing different signals arising due to different levels of interactions [93].*

X-rays are produced when the secondary electrons are ejected from the atomic orbitals leaving vacancies in the electron shell of the specimen atom. Electrons from higher shells fill these vacancies. When electrons from higher electron shells drop down to fill the vacancy, they lose energy in the form of X-rays. These X-rays contain the characteristic energy and wavelength of the atomic orbital of the higher shell, thus containing the characteristic of the atom as well, and are called characteristic X-rays. Apart from this, X-rays are also produced when the electrons in the electron beam lose energy due to deceleration and the lost energy in emitted as X-rays (Bremsstalhung radiation). The X-ray information obtained from SEM is a mix of characteristic (sharp peaks) and Bremsstalhung (spectrum that forms the background) radiations and exist as a continuous electromagnetic spectrum. These characteristic X-rays are used for elemental analysis and chemical composition analysis [22]

7.2 SEM – Subsystems

SEM can be broadly divided into two parts, namely, Microscope Column and Control Console.

The following parts are categorized under microscope column:

Electron gun produces electron beams that are accelerated between 0.1 and 30 keV, with high current, small energy dispersion and extremely small spot size. Several types of electron guns exist, of which tungsten or Lanthanum Hexaboride (LaB_6) cathodes (thermionic sources) belong to older generation SEMs and modern SEMs are provided with field emission sources, with the advantages of lower energy dispersion and enhanced current. Field Emission sources provide 100x greater brightness, much lower electron energy spread (0.3V) and much smaller probe size (2 nm) compared to thermionic sources, resulting in significantly higher resolution and lower chromatic aberrations. The trade-offs include requirement of ultrahigh vacuum ($>10^{-9}$ Torr) and higher cost. [22, 93]

Electron lenses are needed to focus the electron beam to the surface of interest. Magnetic field is used to control the beam, where applied currents to electromagnets help change trajectories of the electrons in the beam. These electron lenses are also used for the magnification or demagnification of the electron beam diameter, resulting in variable focal length. The electron lenses are of two types, condenser, and objective lenses. [93]

Condenser lenses are used to converge and collimate the electron beam that gets diverged when passing from the electron source through the anode plates. A condenser aperture is situated below the condenser lenses, and the focal point of the electron beam is right above this aperture. It is used to remove inhomogeneous and scattered electron from the beam. Modern SEMs usually consist of two condenser lenses for better precision. [93]

Objective lenses are used to focus the electron beam at a point on the surface of the specimen and helps control the size of electron beam. [93]

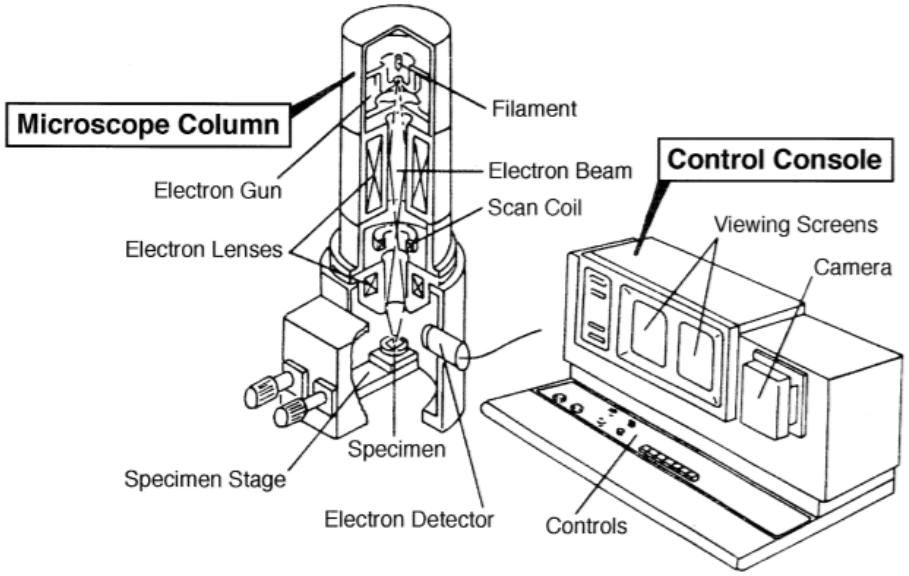

Figure 17: *SEM schematics, major parts – microscope column and control console [22].*

Detectors collect the signal that arises from the beam-specimen interaction. The specimen-beam interaction produces different signals, of which the most important are SE and BSE signals. The different signals generated can be displayed as images, as the electronics in the detector system convert the signal changes into intensity changes on a point-by-point basis. Everhart-Thornley (ET) detector is the standard detector used in most SEMs. It collects both SE and BSE (+300V for SE and BSE, -100 for BSE only) [22, 93].

Operator controls help the operator optimize the image formation through various control options, including accelerating voltage, emission current, lens controls (control of beam current and beam size), focus through objective lens, contrast, and brightness levels of the image. [22]

In this thesis, the surface topography analysis is the focus as it provides useful information on the characterization of the sample specimens. Secondary electrons are basically low energy electrons, an average of around 3-5eV, and they provide information on nanometre scale, that help visualize texture, roughness and other contrasts in topologies of surfaces.

7.3 Factors influencing image quality

To achieve precise image quality, it is important to address the aspects influencing image formation. Fine resolution at high magnifications and good depth of focus allow observeation of features of interest with the best possible quality. There are four main factors that limit the feature visibility and sharpness of the images produced in SEM micrographs, namely:

1. accelerating voltage – electron beam acceleration voltage V_o
2. electron probe current - current that generates various imaging signals upon interaction i_p
3. electron probe convergence angle - depends on the electrons converging onto specimen α_p
4. probe size - electron beam diameter at the specimen surface d_p

(Note: "Electron beam' refers to the electrons present in the column beyond the electron gun at any point.' Electron probe' refers to the electron beam that is focused at the specimen)

To resolve an image into the finest of details, the probe diameter d_p needs to be as small as possible, preferably smaller than or comparable to the feature of interest in the image. The background must have distinguishable contrast from the feature of interest to obtain good visibility and detail for which large probe current i_p is required. At high resolution, with adequately small d_p the image still needs a high i_p to reduce noise and make the image sharp [22, 84].

For a surface with high surface roughness, it is important that the depth of focus is large, so that the different features of the surface with varying heights are all always in focus. To obtain the best depth of focus, it is required that the convergence angle be as low as possible, which enables the beam diameter to avoid divergence over longer distances. This enables the features at different heights to be in focus [22].

Accelerating voltage affects the quality of image when surface features are observed. The beam-electron interaction needs to be confined to surface region of the specimen, to enrich the surface details and low accelerating voltage is the key to achieving this. The trade-off in using low V_o is image resolution. The four beam parameters can be appropriated and optimized to achieve the best possible image for the specific types of surface features [22, 93].

7.4 High resolution imaging at low voltage

High resolution image formation can be efficient using low beam energies between the range 5keV to 500eV. With the reduction of beam energy, the dimensions of interaction volume decrease as the power of ~1.7, hence more signals are obtained from sample surface resulting in high resolution topological features. Some drawbacks with operating at low voltage are the reduction on brightness of the image, due to the reduction in source brightness, which affects the contrast. Contamination is also a concern at low voltages. However, careful choosing of operational parameters and sample preparation, can render this method extremely useful for high resolution imaging. An example of a SEM micrograph of cross-sectioned Silicon

semiconductor device coated with 2nm thick layer of platinum metal at beam energy 9keV is shown in Figure 18. Individual metal particles of sizes up to 1 nm are clearly visible and sufficient topological contrast from semiconductor device is also present [22, 93]. In this thesis, low voltage imaging has been used to obtain most SEM micrographs. An example of SEM micrograph taken during the experimental work of the thesis is shown in Figure 19.

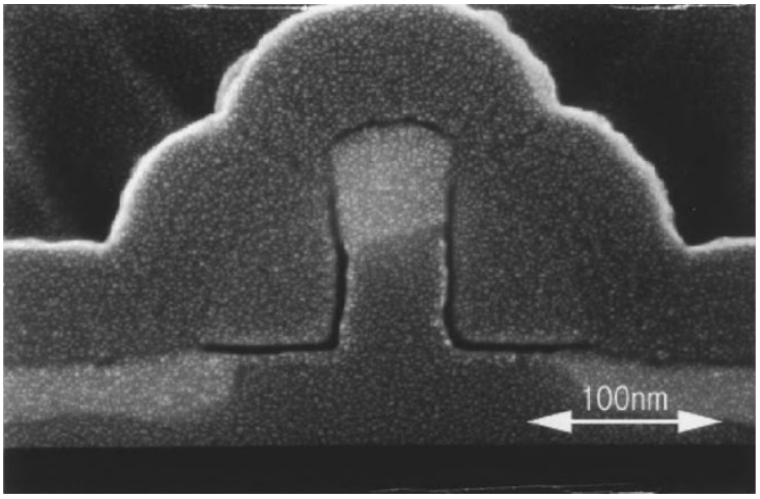

Figure 18: *Cross-sectioned Silicon semiconductor device coated with 2nm thick layer of platinum metal at beam energy 9keV [22].*

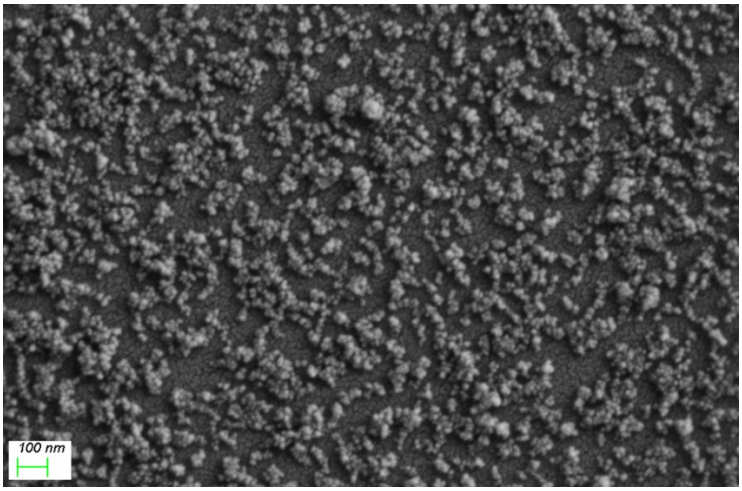

Figure 19: *SEM image of DND on Silicon substrate, taken at 2.80kV with Zeiss Sigma VP SEM in this research experiment work.*

8 Experimental part

The DND coated samples were fabricated using spin coating and automated spray coating technique. The dimension of each sample is 1cm x 1cm x 0.68mm.

8.1 Spin coating

The Si wafers used in all experiments in this work were cleaned by standard RCA procedure. The DND-water suspension with concentration of 5 wt-% was diluted with ethanol to 0.05 wt-%. The solution was ultrasonicated (bandelin sonorex rk 102 h) with 35 kHz for 3 hours. The samples were fabricated by spin coating the DND solution on Si substrate. The Si wafer (1cm x 1cm x 0.68mm) was placed on the spin coater (Laurell ws 650mz 23npp). 60 µl solution was dropped on the Si substrate. The spin coater run at two speeds: 300 rpm for 15 seconds and 2000 rpm for 25 seconds. The sample was then dried on a hotplate at 100°C for 1 minute. The spin coating procedure was performed twice on each sample.

8.2 Automated spray coating

Before the spraying procedure, the required spray height and solution consumption rate are calculated. To calculate the spray height the Equation (6) is used. Since each sample is 10mm in side, the spray coverage is chosen as 10mm. The spray angle of nozzle is 65 degrees. Using the formula, the spray height is calculated to be 8mm. The z axis of the device is moved in the forward direction by 8mm to fix the spray height. The consumption rate of the solution is experimentally calculated to by 133 µl/cm based on the initial and final solution volumes, and the distance covered by spraying. The DND-water suspension with concentration of 5 wt-% was diluted with ethanol to 0.05 wt-%. The solution was ultrasonicated bandelin sonorex rk 102 h) with 35 kHz for 3 hours. The glass plate of the spraying device was heated to 55°C. The samples were placed on the glass plate, three at a time, and the spraying was performed twice on each sample.

8.3 Sample preparation for SEM analysis

8.3.1 Cross-section preparation

Direct cross-sections were prepared by cleaving the DND coated Si samples in half with the use of diamond scriber.

Epoxy embedded samples were prepared due to unsuccessful thickness measurement from direct cross-section measurement. The samples were cleaved in half after DND deposition and each half was embedded in epoxy. Epoxy was prepared by mixing 7.5ml of epoxy resin (Epo Fix) with 1ml of hardener (Epo Fix), for each sample. The samples were placed inside a mould and epoxy mixture was poured into the mould carefully, to not directly touch the DND coated surface. Samples were then left to harden overnight.

The embedded samples were then ground and polished to get the SEM-ready samples. For grinding, sand papers (BUEHLER Silicon carbide) of three different grades were used. 320p which is the roughest was used first followed by 1000p and 2500p. This was followed by polishing using Struers RotoPol-22 polisher. Polishing consisted on two steps. In the first step, 6µm cloth was used with 6 µm diamond paste. The polishing was performed at 50N for 5 minutes followed by 30N for 1 minute. In the second step, 1 µm cloth was used with 1 µm diamond paste and polishing was performed at 20N for 5 minutes followed by 15N for 2 minutes. The polished samples were then sputter coated using the following method.

8.3.2 Sputter coating

For SEM analysis the samples need to be made conductive to avoid interference in image formation caused due to the high accelerating voltage. This is achieved by sputter coating the samples with Platinum. The samples were placed in a sputtering device (Emitech K100X) and the device was run for a minute with actual current of 20mA (set current 30mA) and vacuum of 6 x 10^{-2} Torr. The platinum is sputtered onto the sample surface, creating an 7nm thick Platinum layer on the surface (see Figure 20).

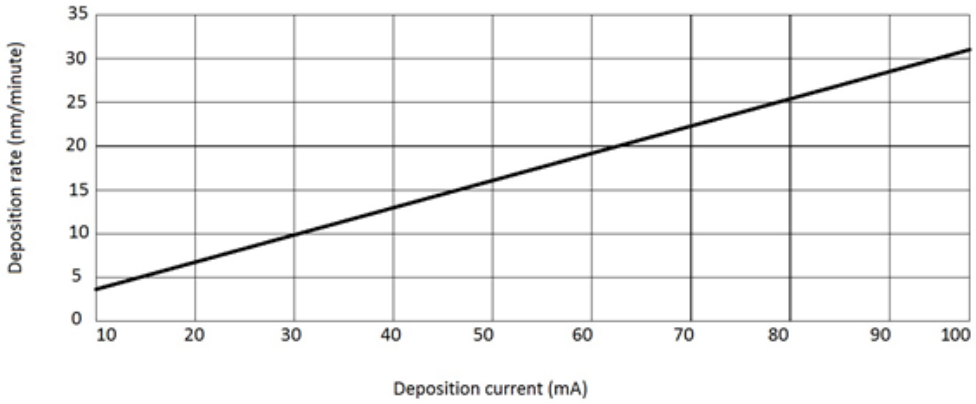

Figure 20: *Sputter deposition graph showing sputtering deposition rate with respect to deposition current (Emitech K100X).*

The cross-sectioned and sputter coated samples were attached to SEM stubs using carbon tapes. A thin conductive copper strip was used to connect the embedded sample surface to the surface of the stub. The SEM analysis was performed using Zeiss Sigma VP with Schottky FEG emitter. The microscope was operated in high vacuum mode (10^{-7} mbar) and SE (Secondary Electron) detector and In Lens detector were used to obtain the micrographs. Distribution and agglomeration analysis, and thickness measurements were performed with SEM, on both spin coated and spray coated samples.

9 Results

9.1 Distribution

Visual examination of the samples at microscale and nanoscale reveals that for the same amount of solution consumption (266µl/cm), particle density is much higher in spray coated sample (S2) compared to spin coated sample (S1) (Figure 21).

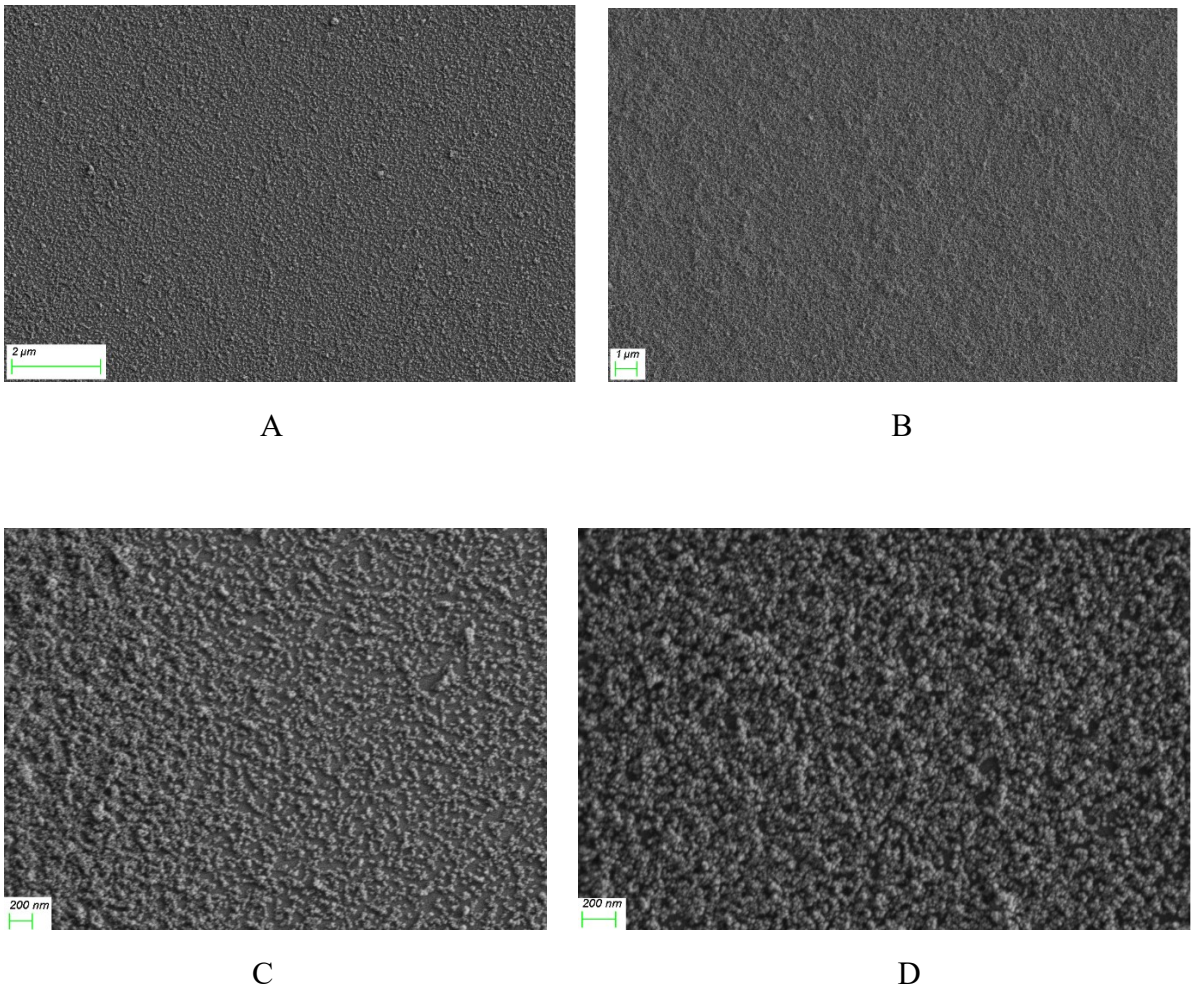

Figure 21: *SEM image of A) spin coated sample S1 at microscale (EHT=2.80kV, SE2 detector) B) spray coated sample S2 at microscale (EHT=1.60V, SE2 detector) C) particle density distribution of spin coated sample S1 (EHT=2kV, SE2 detector), D) particle density distribution of spray coated sample S2 (EHT= 1.60kV, SE2 detector)*

9.2 Agglomeration

9.2.1 Size distribution

Spin coating procedure does not alter the agglomeration of the DND particles. Since spin coated samples had low particle density, the surface of the Silicon substrate was visible in the micrograph. This provided improved contrast on the micrograph and so spin coated sample (S3) were used to analyse the size distribution of the DND particles.

Zeiss Sigma VP has an inbuilt software (Zeiss ZEN) to measure the distance between two points on the micrograph. The image analysis software Image J is used for further analyses, like size distribution calculation. Figure 23 shows the size distribution histogram for the selected area (yellow square in Figure 22). The size distribution is approximate because the analysis software does not detect agglomerates with highly irregular shape. To get more accurate size distribution the diameter of 150 agglomerates were measured manually for the same area (see Figure 24).

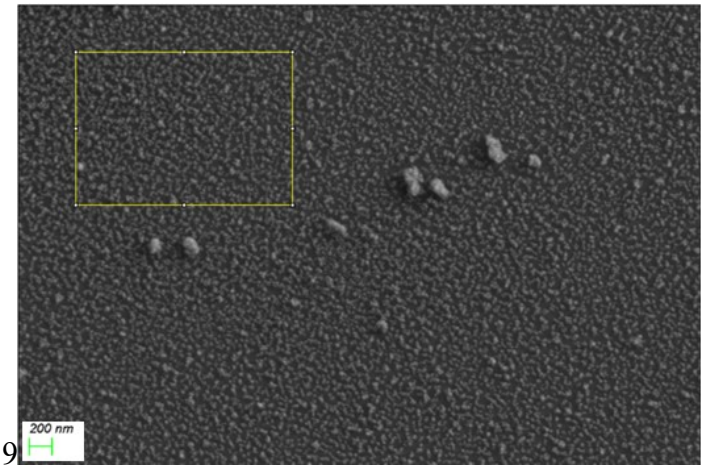

Figure 22: *SEM image of spin coated sample S3 (EHT=3kV).*

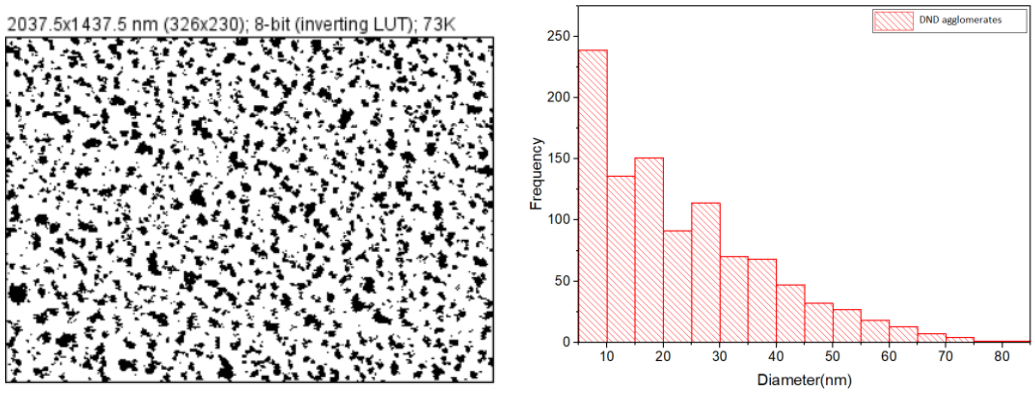

Figure 23: *Agglomerate size measurement – processed image (left), size distribution histogram (right).*

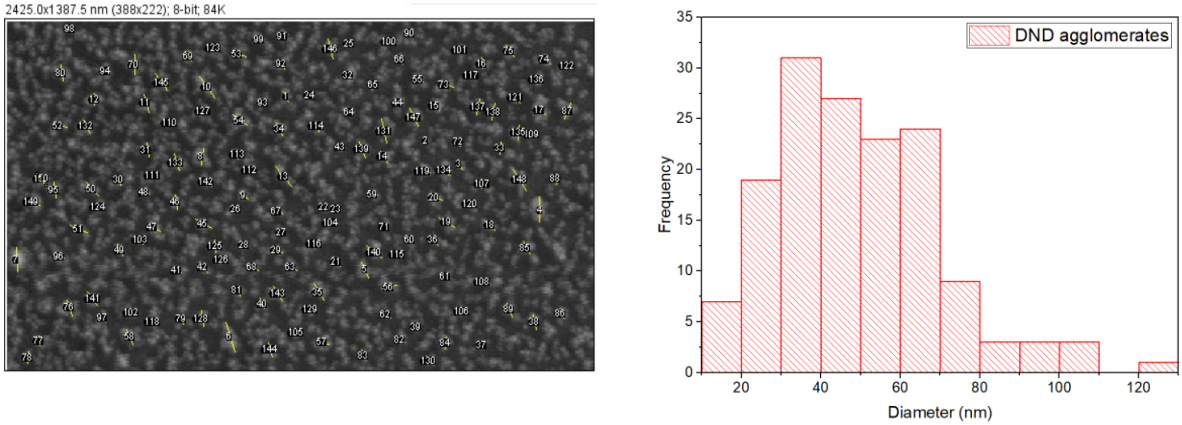

Figure 24*: Agglomerate size measurement - manual (left), size distribution histogram (right).*

9.2.2 Observation of primary particles

For observing primary particles, it is necessary to go to high resolutions, and the best setting was found to be low voltage-high resolution setting. The SE2 detector could not go beyond the 100-nm scale (Figure 25). In order to go below 100 nm, In-Lens detector present in Zeiss Sigma VP was used. In-Lens detector collects SE signals as well as BSE signals, providing better resolution and contrast at nanoscale. Figure 26 shows the SEM image taken using In-lens detector. 10 particles were analysed, with the aim of measuring the smallest particle diameter. The summary of the observed particles in shown in table. The minimum observable particle size is ~ 11 nm.

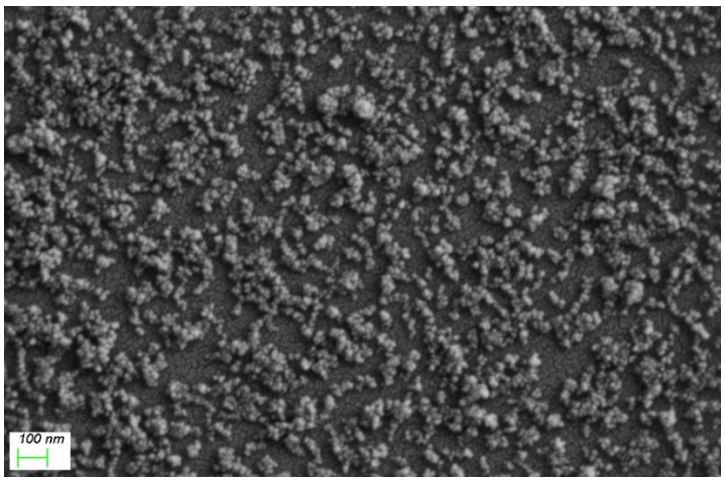

Figure 25: *SEM image of spin coated sample S4 (EHT=1.60kV, SE2 detector).*

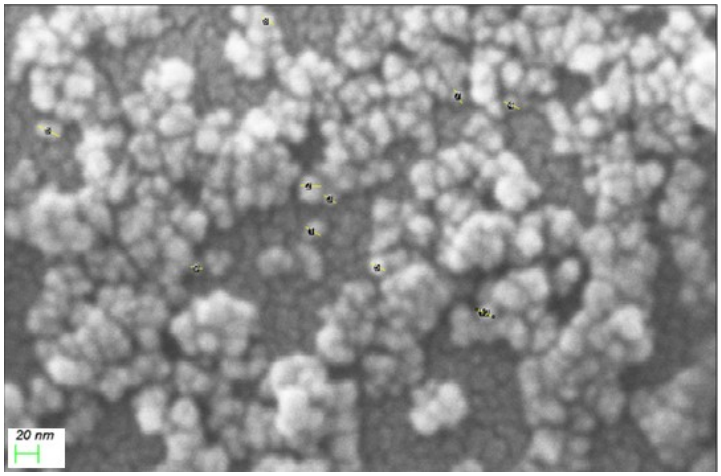

Summary	~ Diameter (nm)
Mean	15
Min	11
Max	22

Figure 26: *SEM image EHT = 2.20kV, In-Lens detector(up), summary of single particle diameter(down).*

The main problem with high resolution imaging is the destruction of samples, even at low voltages. The images need to be taken within a very short time frame, typically within a few seconds to preserve the samples, which was challenging. Figure 27 shows SEM image of destroyed sample.

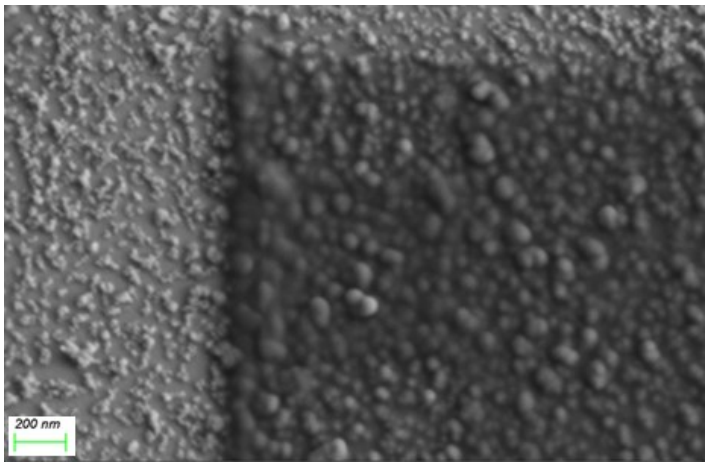

Figure 27: *SEM image spin coated sample S5, (EHT = 1.4kV, SE2 detector).*

9.3 Thickness measurement

Thickness measurement was performed with both spin coated and spray coated samples, using the same amount of solution per unit area for both techniques. Three samples T1, T2 and T3 were fabricated using the spray coating technique and two samples T4 and T5 were fabricated using the spin coating technique (Figures 28-29).

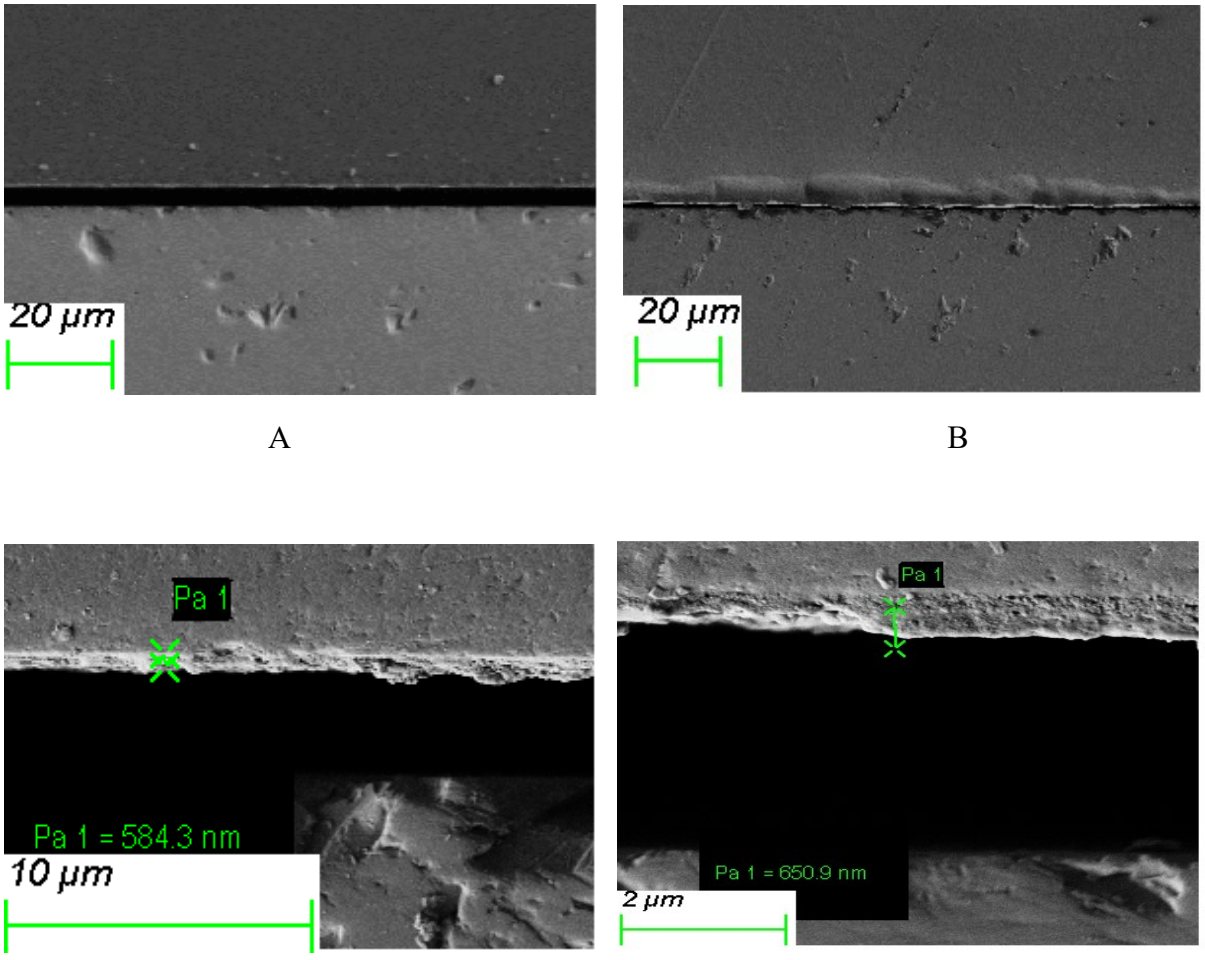

Figure 28: *A) Cross-section of spray coated sample T1 (EHT = 2.2 kV, SE2 detector), B) cross-section of spin coated sample T4 (EHT = 3 kV, SE2 detector), C) cross-section of spray coated sample T1 (EHT=2.00kV, SE2 detector), D) cross-section of spray coated sample T2 (EHT = 2.00kV, SE2 detector).*

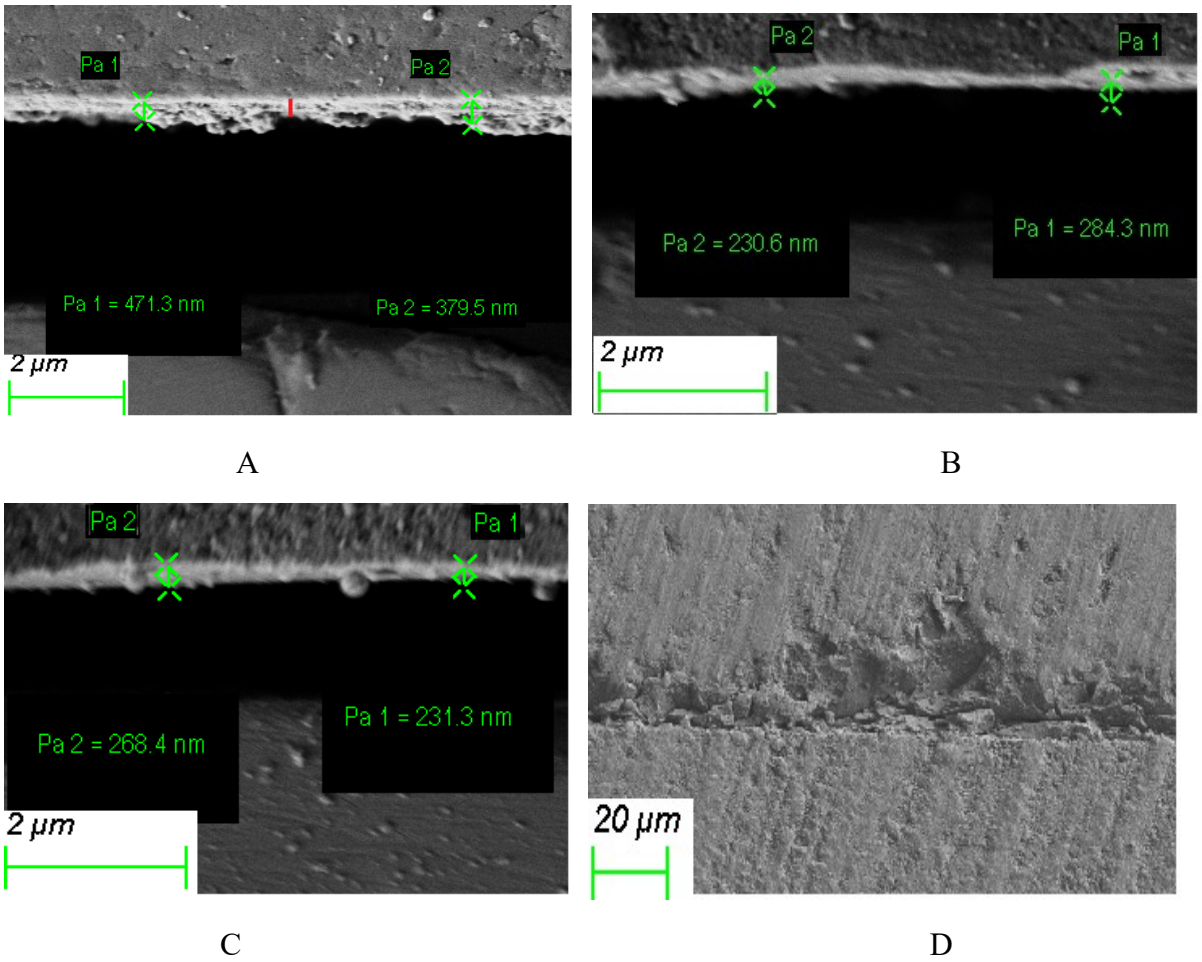

Figure 29: *A) Cross-section of spray coated sample T3 (EHT = 2.00kV, SE2), B) cross-section of spin coated sample T4 (EHT = 2.0 kV, SE2 detector), C) cross-section of spin coated sample T5 (EHT = 2.2kV, SE2 detector), D) cross-section of spray-coated sample without grinding and polishing process (EHT = 3kV, SE2 detector).*

The major problem in the above measurement is that, the polishing and grinding process involved in the SEM sample preparation causes extreme stress to the sample surface and the DND coating is completely delaminated from the surface as a result. Although the thickness could be measured, it is not entirely reliable. To avoid delamination, the grinding and polishing processes were excluded. The samples were embedded in epoxy resin and the surface of the cross-section (the surface where thickness is measured) was evened out using sand paper of grade 320p. The results are as shown in the Figure 29 D.

Although the DND coating was not delaminated, it was very difficult to measure the thickness of the sample reliably, without having a polished surface. Thorough grinding and polishing of the cross-sectional surface seems to be better for thickness measurement.

10 Discussion

It was challenging to find the appropriate sample preparation method for measuring film thickness using SEM imaging. Various sample preparation methods discussed below were employed in order to obtain reliable sample cross-sections for SEM analysis. The different sample preparation and measurement methods experimented in this work are listed in the Table 9.

Direct cross-section measurement: Initially cross-sectional samples were obtained by scribing and cleaving the DND coated Si sample in half, using diamond scriber. The SEM measurements for these samples showed little contrast between the coating and substrate and hence thickness measurement was unsuccessful. To improve contrast, oxidized Si wafer with oxide layer of 300nm (obtained from Micronova cleanroom) was used. The contrast seemed to improve slightly with the oxide layer, but it was still not possible to differentiate clearly between the Si substrate layer, oxide layer and the DND thin film layer. However, the major problem with the direct measurement of cleaved samples was the presence of highly uneven facets due to imperfect cleaving. The DND coating on the Si surface further deteriorated the quality of cleaving. Therefore, it was necessary to polish the Si surface after cleaving.

Epoxy embedded cross-section measurement: To obtain polished cross-sectional samples, DND coated samples were cleaved in half and embedded in epoxy. The hardened epoxy embedded samples were then grinded and polished to obtain smooth cross-sectional surfaces. SEM imaging of these samples revealed complete delamination of the coating from Si surface. This is expected to occur due to the intense grinding and polishing process during sample preparation. In order to prevent delamination, a 20nm layer Pt film was deposited on the sample using sputter coating device before embedding process. This was followed by epoxy embedding, grinding and polishing protocols similar to the previous set of samples. SEM analysis of these samples showed that it was not possible to prevent delamination using this method. It is expected that a thicker layer (>100nm) of metal coating might help in preventing delamination. In this work, it was not possible to deposit thicker layer of metal due to sputtering device constraints.

Table 9: *Different SEM sample preparation methods and alternative sample measurement methods used in this thesis.*

SEM analysis	Comments
Direct cross-section measurement (DND on Si)	Low contrast between coating and substrate, extremely uneven facets at cross-section
Direct cross-section measurement (DND on oxidized Si (300nm oxide layer))	Slightly improved contrast between substrate and coating, extremely uneven facets at cross-section
Cross-section measurement with DND on Si embedded in epoxy	Very good contrast between Si, DND and epoxy layers, complete delamination of DND film from Si
Cross-section measurement with sputter coated DND on Si embedded in epoxy	Very good contrast between Si, DND and epoxy layers, complete delamination of DND film from Si, no improvement in delamination
SEM+EDX (Elemental mapping done using analytical field emission SEM - JEOL JSM-7500FA)	Carbon contamination, no clear differentiation between different layers
Non-invasive analysis	
Spectroscopic ellipsometry	Thin film inhomogeneity caused air pockets on sample surface rendering the measurement results inaccurate

Alternative measurement methods: SEM with Energy dispersive spectroscopy X-ray spectroscopy was considered as an alternative measurement tool for the thickness measurements. The cross-sectional area analysis was performed using the elemental mapping mode in JEOL JSM-7500FA field emission SEM. This method uses the X-rays generated in SEM to obtain atomic information (Chapter 7). The SEM+EDX analysis was unable to clearly differentiate the Si surface and DND coating, due to carbon peaks existing all over the sample cross-section. This could be due to contamination of the sample surface and the vacuum chamber. Further analysis with EDX was increasingly complicated, which defeated the purpose of the work to find a less complicated analysis tool.

Spectroscopic ellipsometry, a non-invasive tool was considered as the next alternative. The thickness measurement was largely unsuccessful due to the absence of homogenous sample surface. The inhomogeneity is expected to occur due to agglomeration of the DND particles, which causes pockets of air trapped on the sample surface. The ellipsometer possibly detected the air, and as a result the measured refractive index was very close to that of air (n=1) than that of the DND (n=2.55 [7]). This resulted in inaccurate thickness measurement results. This method may possibly work when extremely homogenous DND coatings are fabricated.

Of the above methods, SEM cross-sectional analysis with samples embedded in epoxy had good differentiation between the different layers (Si, DND and epoxy layers). The SEM micrographs of thickness measurement from epoxy-embedded samples are shown in Figures 28-29.

The SEM images were analysed using Image J to obtain the thickness measurements. For each sample, 20 measurements were made. The outliers (longest and shortest measurements) were excluded to obtain the mean thickness and standard deviation values. From the thickness measurement results (Table 10), it is observed that the spray coated samples have an average thickness between 450-500 nm. The coating thickness is uneven in several places, from Figure (28-29), which could be due to the agglomeration of particles. In this thesis, ultrasonication is used as the primary deagglomeration method (Chapter 4). It was not possible to break the core aggregates into primary particles or single digit particles using ultrasonication.

Table 10: *Thickness measurements of samples fabricated using spin coating and automated spray coating technique.*

Summary	**~ Length(nm)**				
Fabrication method	**Spray coating using automated spray coating technique**			**Spin coating**	
Sample ID	**T1**	**T2**	**T3**	**T4**	**T5**
Mean	500	547	444	241	227
Min	392	464	326	180	126
Max	606	607	559	292	344
SD	74	43	73	38	66
Longest	1176	893	816	450	399
Shortest	325	254	232	145	163

Other deagglomeration methods like centrifugation, wet stirred media milling and bead assisted sonic disintegration produce deagglomeration resulting in single digit nanodiamond particles, which might improve the evenness of the thin film coating. The sample preparation for thickness measurement involves intense grinding and polishing processes, which tend to completely delaminate the coating from the surface of the Silicon substrate. Excluding grinding

and polishing steps result in highly uneven cross-section. The use of sand paper to even out the cross-section contaminates the surface further. Thus, it becomes very difficult to measure the thickness. Comparatively, grinding and polishing leads to cleaner samples and better observation in SEM. The spray coating technique has been tested with samples T1, T2 and T3. The thickness measurements of the three samples vary only by a few tens of nanometres. The spin coated samples have an average thickness of between 200 – 250 nm, for the same amount of solution used. The lower value of thickness is because a part of the solution is flung away from the substrate during the spin coating process, causing solution wastage.

SEM provides micrographs with good resolution for the thickness analysis. However, the sample preparation methods for the SEM analysis of DND thin film coated samples were unsuccessful due to delamination. Alternative sample preparation methods for the preparation of sample cross-sections might provide results that are more reliable. Alternative substrate material that has better adhesion with DNDs might help prevent delamination. Sealing DND film on the substrate surface with a few hundred nanometres thick metal as top coating might help the DND film to stay intact on the substrate. Avoiding intense grinding and polishing by using suitable cutting tools as an alternative might prevent delamination.

The thickness measurement results produced for the SEM micrographs are not accurate. The epoxy surface might be porous and uneven which further reduces the accuracy of the thickness measurement. However, by averaging the thickness measurements obtained from several points of cross-section, an approximate thickness value can be obtained. With improved sample preparation methods and homogeneity of sample surfaces, thickness results are expected to improve in accuracy.

11 Conclusion

SEM is a suitable analysis tool for measuring the thickness of thin film coatings, as it provides good resolution at high magnifications, and good contrast between Silicon substrate and the DND particles. However, preparing suitable cross-section of the samples was very challenging. The various sample preparation methods used in this work were not suitable for producing accurate thickness measurement results. Other sample preparation methods like focused ion beam (FIB) which is the sample preparation method used for TEM, can be used to get suitable cross-sections for SEM, but it is complicated and expensive. TEM has been commonly used for the observation of DND primary particles. The sample preparation in TEM is tedious and costly, which are trade-offs in comparison to using SEM where sample preparation is relatively simple, and the method is relatively less expensive. Effective sample preparation methods for SEM may possibly improve the accuracy of the thickness measurement results from SEM analysis.

With improved deagglomeration techniques, the automated spraying device is suitable to make thin film coatings of DND particles. However, further experimentation is required to test the reliability of such samples to be used in biomedical applications. Depending on the application and requirement, parameters such as interfacial adhesion, wettability, elastic modulus, thermal expansion coefficient and mechanical stress of the thin films need to be tested extensively. DND is a potential candidate for biological applications because of its biocompatibility, and suitable chemical, optical and mechanical properties. Extensive and exclusive application-specific research is required to potentially use DNDs as thin film coatings in various biological and biomedical applications.

Acknowledgement

The experimental part of the thesis was carried out at laboratories in Micronova Nanofabrication Centre, supported by Aalto university.

The samples and technical equipment were provided by Microsystem technology research group, Aalto university.

The SEM images were taken using the facilities and technical support by Aalto University at OtaNano - Nanomicroscopy Center (Aalto-NMC)

References

[1] M. Schrand, S. A. C. Hens, O.A. Shenderova, "Nanodiamond Particles: Properties and Perspectives for Bioapplications*", Critical Reviews in Solid State and Materials Sciences*, vol. 34, issue 1-2, p. 18-74, 2009.

[2] A. Prasad, K. Mahato, "Biomaterials for Biosensing Applications", *Journal of Analytical and Bioanalytical techniques*, vol. 7, issue 2, 2016.

[3] M. Niemeyer, Christof, "Nanoparticles, Proteins, and Nucleic Acids: Biotechnology Meets Materials Science", *Angewandte Chemie int. ed*., vol. 40, p. 4128-4158, 2001.

[4] P. Vadgama, "Surfaces and Interfaces for biomaterials", *CRS Press LLC*, 2005.

[5] R. Peterson, "Carbon Fiber Biocompatibility for Implants", *Fibers, PMC*., vol. 4, 2016.

[6] T. Laurilaa, S. Sainio, M. A. Caro," Hybrid carbon-based nanomaterials for electrochemical detection of biomolecules", *Progress in material science, Elsevier*, vol. 88, p. 499-594, 2017.

[7] O.A. Shenderova, V.V. Zhirnov, D.W. Brenner, "Carbon nanostructures", *Critical Review of Solid State Material Science.,* vol. 27, issue. 227, 2002.

[8] W. Yang, O. Auciello, J.E. Butler, W. Cai, J. A. Carlisle, "DNA-modified nanocrystalline diamond thin films as stable, biologically active substrates", *Nature materials*, vol.1, p. 253-257, 2002.

[9] L.C.L. Huang, H.C. Chang, "Adsorption and Immobilization of Cytochrome c on Nanodiamonds", *American Chemical Society*, vol. 20, issue. 14, p. 5879-5884, 2004.

[10] E. Kaivosoja, S. Sainio, J. Lyytinen, T. Palomäki, T. Laurila, S. I. Kim, J. G. Han, and J. Koskinen, "Carbon thin films as electrode material in neural sensing*", Surface and Coatings Technology*, vol. 259, pp. 33–38, 2014.

[11] O.A. Schenderova, "Nanodiamonds Shine New Light on Bio Applications", *BioPhotonics*, p. 8-9, 2015

[12] T. S. Huangae, Y. Tzengbe, Y. K. Liuca, Y. C. Chenbe, K. R. Walkerae, R. Guntupallide, C. Liu, "Immobilization of antibodies and bacterial binding on nanodiamond and carbon nanotubes for biosensor applications", *Diamond and related materials*., vol.13, issue. 4-8, p. 1098-1102, 2004.

[13] D. L. Robinson, B. J. Venton, M. L. Heien, and R. M. Wightman, "Detecting subsecond dopamine release with fast-scan cyclic voltammetry in vivo," *Clinical chemistry*, vol. 49, no. 10, pp. 1763–1773, 2003.

[14] M. Khan, "Dispersion behaviour and the influences of ball milling technique on functionalization of detonated nano-diamonds.", Diamond and Related Materials, vol. 61, p. 32 – 40, 2016.

[15] M. Eslamian, "A Model for the Fabrication of Polymer Solar Cells by Spray Coating." *Drying Technology*, vol. 22 p. 405–413, 2013.

[16] P. V. Lebedev-Stepanov, S. P. Molchanov, A. L. Vasil'evc, V. P. Mitrokhina, G. A. Yurasika, A. E. Aleksenskiid, A. T. Dideikin, "Formation of nanodiamond films from aqueous suspensions during spin coating", *Technical physics*., vol. 61, no. 3, p. 401-498, 2016.

[17] L. Besra, M. Liu, "A review on fundamentals and applications of electrophoretic deposition (EPD)", *Progress in material science*, vol. 52, issue 1, p. 1-61, 2007.

[18] R. J. Edgington1, A. Thalhammer, J. O. Welch, A. Bongrain, P. Bergonzo, E. Scorsone, R. B. Jackman,R Schoepfer, "Patterned neuronal networks using nanodiamonds and the effect of varying nanodiamond properties on neuronal adhesion and outgrowth", *Journal of Neural Engineering*, vol. 10, no. 5, 2013.

[19] R. Narayan, "Diamond-based materials for biomedical applications", *Woodhead publishing, 2003.*

[20] H. J. Griesser, "Thin film coatings for biomaterials and biomedical applications", *Elsevier*, 2016.

[21] S. Stehlik, M. Varga, P. Stenclova, L. Ondic, M. Ledinsky, J. Pangrac, O. Vanek, "Ultrathin Nanocrystalline Diamond Films with Silicon Vacancy Color Centers via Seeding by 2 nm Detonation Nanodiamonds*", ACS Appl. Mater. Interfaces*., vol. 9, issue. 44, p. 38842–38853, 2017.

[22] J. I. Goldstein, C. E. Lyman, D. E. Newbury, E. Lifshin, “Scanning Electron Microscopy and X-ray Microanalysis”, *United States of America: Springer publication*, 2003.

[23] M. Huitle, “Diamond Microelectrodes and their Applications in Biological Studies”, *Small.*, vol. 3, issue. 9, p. 1474-1476, 2007.

[24] M. D. Angione, R. P. Serafina, C. M. Magliulo, “Carbon based materials for electronic bio-sensing”, *Materials today*., vol. 14, issue. 9, p. 424-433, 2001.

[25] B. M. Holzapfel, J. C. Reichert, “How smart do biomaterials need to be? A translational science and clinical point of view”, *Advanced drug delivery reviews*., vol. 65, issue. 4, p. 581-603, 2013.

[26] D. Ho, “Nanodiamonds: Applications in biology and nanoscale medicine. S.I”, *Springer,* 2010.

[27] P. S. Mead, L. Slutsker, V. Dietz, L. F. McCaig, J. S. Bresee, C. Shapiro, “Food-related illness and death in the United States”, *Emerging Infectious Diseases*, vol. 5, p. 607-625, 1999.

[28] S. Stehlik, T. Petit, H. Girard, J. Arnault, J, A. Kromka, “Nanoparticles Assume Electrical Potential According to Substrate, Size, and Surface Termination”, Langmuir, vol. 29, issue. 5, p. 1634– 164, 2013.

[29] J.M. Beaulieu, R.R. Gainetdinov,” *The Physiology, Signaling, and Pharmacology of Dopamine Receptors” Pharmacological Reviews*., vol. 63, no. 1, p. 182-217, 2011.

[30] S. Little, P. Brown, Ann. N. Y.” What brain signals are suitable for feedback control of deep brain stimulation in Parkinson's disease?”, *Acad. Sci*., vol. 1265, no. 1, 2012.

[31] E. Leppänen, “Electrochemical characterization of tetrahedral amorphous carbon and detonation nanodiamond hybrid electrode for detection of dopamine”, *master’s thesis*, 2017.

[32] V. Y. Dolmatov, “Detonation-synthesis nanodiamonds: synthesis, structure, properties and applications*”, Russian Chemical Reviews*., vol. 76, issue. 4, 2007.

[33] R. Peterson, “Carbon Fiber Biocompatibility for Implants”, Fibers, vol. 4, issue. 1, 2016.

[34] O. A. Shenderova, D. M. Gruen, “Ultrananocrystalline Diamond - Synthesis, Properties, and Applications”, *William-Andrew, Norwich, NY*, 2006.

[35] B. I. Kharisov, O. V. Kharissova, L. C. Guerrere," Synthesis Techniques, Properties, and Applications of Nanodiamonds", *Synthesis and Reactivity in Inorganic, Metal-Organic, and Nano-Metal Chemistry,* vol. 40, issue 2, p. 84-101, 2010.

[36] V.V. Danilenko, "On the history of the discovery of nanodiamond synthesis", *Physics of Solid State*, vol. 46, issue. 595, 2004.

[37] O. A. Shenderova, D. M. Gruen, "Ultrananocrystalline Diamond - Synthesis, Properties, and Applications", *Elsevier*, 2012.

[38] V.V. Danilenko, "On the discovery of detonation nanodiamond, in O.A. Shenderova, D.M. Gruen (Eds), Ultrananocrystalline Diamond, *William Andrew, Norwich, NY*, p. 335–344, 2006.

[39] A. M. Staver, A. I. Lyamkin, N. A. Gubareva, E. A. Petrov, "Ultradisperse diamond powders produced by explosion", *Fiz. Goren. Vzryva*., vol. 20 no. 5, p. 100–103, 1984.

[40] N. Roy Greiner, P. S. Philips, J. D. Johnson, "Diamond in detonation soot", *Nature*, vol. 333, p. 440-442, 1988.

[41] J. Lee, J. Kim, J. Kim, H. Kang, "Novel electrode for water purification based on nano-fication based on nanodiamonds", *The Electrochemical Society*., 2011.

[42] R.A. Freitas, Biocompatibility, Nanomedicine, Vol. IIA, *Landes Bioscience,* 2003.

[43] A. L. Vereshchagin, G. S. Yur'ev, "Structure of Detonation Diamond Nanoparticles", *Inorganic materials*., vol. 39, issue. 3, p. 247-253, 2003.

[44] L. Schmidlin, V. Pichota, M. Cometa, S. Josseta, P. Rabub, D. Spitzer, "Identification, quantification and modification of detonation nanodiamond functional groups", *Diamond and related materials*., vol. 22, p. 113-117, 2012.

[45] A. L. Vereshchagin, G. V. Sakovic, "Structure of detonation nanodiamonds*", Mendeleev Communications*, vol. 11, issue. 1, p. 39-41, 2001.

[46] A. Ya. Vul', A. E. Aleksenskiy, and A. T. Dideykin, "Detonation Nanodiamonds: Technology, properties and applications", *Nanosciences and nanotechnologies*., 2018.

[47] K. Mitsuishi, K.I, K. Furuya," High-resolution electron microscopy of detonation nanodiamond", *Nanotechnology*, vol. 10, no.15, 2008.

[48] O. A. shenderova, G. E. Mcguire, "Science and engineering of nanodiamond particle surfaces for biological applications (Review)", *Biointerphases.*, vol. 10, no. 3, p. 030802, 2015.

[49] A. Krüger, "Unusually tight aggregation in detonation nanodiamond: identification and disintegration", *Carbon.*, vol. 43, no. 8, p. 1722 – 1730, 2005.

[50] D. L. Robinson, A. Hermans, A. T. Seipel, and R. M. Wightman, "*Monitoring rapid chemical communication in the brain*," Chemical reviews, vol. 108, no. 7, p. 2554–2584, 2008.

[51] V. Y. Dolmatov, "The up-to-date commercial production process for detonation nanodiamonds, *Report 1",* 2006.

[52] A. Krueger, "The structure and reactivity of nanoscale diamond", *Journal of material chemistry*, vol. 18, p. 1485-1492, 2008.

[53] A. Krueger, D. Lang, "Functionality is key: recent progress in the surface modification of nanodiamond", *Advanced Functional Materials*., vol. 22, p. 890 – 906, 2012.

[54] S. C. Hens, G. Cunningham, T. Tyler, S. Moseenkov, V. Kuznetsov, O. Shenderova, "Nanodiamond bioconjugate probes and their collection by electrophoresis", *Diamond related matter.*, vol. 17, p. 1858–1866, 2008.

[55] A. Krueger, YJ. Liang, G. Jarre, J. Stegk, "Surface functionalisation of detonation diamond suitable for biological applications", *Materials Chemistry*., vol. 16, issue. 24, p. 2322–2328, 2006.

[56] A. Aaleksenskiy, E. Eydelman, A.Y. Vul, “Deagglomeration of detonation nanodiamonds”, *Nanoscience and Nanotechnology Letters*., vol. 3, no. 1, p. 68 – 74, 2011.

[57] K. Turcheniuk, C. Trecazzi, C. Deeleepojananan, V. N. Mochalin, “Salt-Assisted Ultrasonic Deaggregation of Nanodiamond”, *ACS Applied materials and interfaces*., vol. 8, no. 38, p. 25461-25468, 2016.

[58] E. Osawa, “Recent progress and perspectives in single-digit nanodiamond*”, Diamond and Related Materials.*, vol. 16, issue. 12, pp. 2018 – 2022, 2007.

[59] Y. Lang, M. Ozawa, A. Krueger, “A general procedure to functionalize agglomerating nanoparticles demonstrated on nanodiamond”, *ACS nano*., vol. 3, no. 8, p. 2288 – 2296, 2007.

[60] A. Kruger, “New carbon materials: Biological Applications of functionalized nanodiamond materials”, *Chemistry- European Journal*, vol. 14, issue. 5, 2008.

[61] A.M. Schrand, J. Johnson, L. Dai, S.M. Hussain, J.J. Schlager, L. Zhu, “Cytotoxicity and genotoxicity of carbon nanoparticles, in T. Webster (Ed.), Safety of Nanoparticles: From Manufacturing to Clinical Applications”, *Springer Publishing, Brown University*, 2008.

[62] A.M. Schrand, L. Dai, J.J. Schlager, S.M. Hussain, E. Osawa, “Differential biocompatibility of carbon nanotubes and nanodiamonds”, *Diamond and Related Materials*, vol. 16, p.2118, 2007.

[63] A.M. Schrand, H. Huang, C. Carlson, J.J. Schlager, E. Osawa, S.M. Hussain, “Are diamond nanoparticles cytotoxic?”, *Journal of Physical Chemistry*., vol. 111, issue. 2, 2007.

[64] A. Morozan, L. Stamatin, F. Nastase, A. Dumitru, S. Vulpe, C. Nastase,” The biocompatibility microorganisms-carbon nanostructures for applications in microbial fuel cells”, *Physica Status Solidi*., vol. 204, issue. p. 1797–1803, 2007.

[65] S.J. Yu, M.W. Kang, H.C. Chang, K.M. Chen, Y.C. Yu, “Bright fluorescent nano-fluorescent nanodiamonds: no photobleaching and low cytotoxicity”, *Journal of the American Chemical Society*., vol. 127, p. 17604-177605, 2005.

[66] A. Magrez, S. Kasas, V. Salicio, N. Pasquier, J.W. Seo, M. Celio," Cellular toxicity of carbon-based nanoparticles", *Nano Letters*., vol. 6, p. 1121-1125, 2006.

[67] Y. Sato, A. Yokoyama, K. Shibata, Y. Akimoto, S. Ogino, Y. Nodasaka, "Influence of length on cytotoxicity of multi-walled carbon nanotubes against human acute monocytic leukemia cell line THP-1 in vitro and subcutaneous tissue of rats in vivo", *Molecular Biosystems*, vol. 1, issue 2, 2005.

[68] H. Huang, E. Pierstorff, E. Osawa, D. Ho," Active nanodiamond hydrogels for chemotherapeutic delivery", *Nano Letters*., vol. 7, no.11, p.3305–3314, 2007.

[69] S. Vial, C. Mansuy, S. Sagan, T. Irinopoulou, F. Burlina, J.P. Boudou, "Peptide-grafted nanodiamonds: preparation, cytotoxicity and uptake", *Chembiochem*., vol. 9, issue. 13, p. 2113–2119, 2008.

[70] R. Silbajoris, J.M. Huang, W.-Y. Cheng, L. Dailey, T.L. Tal, I. Jaspers," Nanodiamond particles induce Il-8 expression through a transcript stabilization mechanism in human airway epithelial cells", *Nanotoxicology*., vol. 3, issue 2. p.152–160, 2009.

[71] Y. Xing, W. Xiong, L. Zhu, "DNA damage in embryonic stem cells caused by nanodiamonds", *ACS Nano*., vol. 5, no. 3, p. 2376–2384, 2011.

[72] V.Y. Dolmatov, L.N. Kostrova, "Detonation-synthesized nanodiamonds and the feasibility of developing a new generation of medicinals", *Superhard Mater*., vol. 3, p. 82-85, 2000.

[73] R.L. Tse, P. Phelps, "Polymorphonuclear leukocyte motility in vitro. V. Release of chemotactic activity following phagocytosis of calcium pyrophosphate crystals, diamond dust, and urate crystals", *J. Lab. Clin. Med.,* vol. 76, p. 403-415, 1970.

[74] H. Eidi "Fluorescent nanodiamonds as a relevant tag for the assessment of alum adjuvant particle biodisposition", *BMC medicine*., vol. 13, no.1, p. 144, 2015.

[75] G. Jia, H. Wang, L. Yan, X. Wang, R. Pei, T. Yan, Y. Zhao, X. Guo, "Cytotoxicity of carbon nanomaterials: Single-wall nanotube, Multi-wall nanotube and fullerene" *Environmental Science and Technology*., vol. 39, no. 5, p. 1378-1383, 2005.

[76] A. Magrez, S. Kasas, V. Salicio, N. Pasquier, J.-W. Seo, M. Celio, S. Catsicas, B. Schwaller, L. Forro, "Cellular Toxicity of Carbon-Based Nanomaterials", *Nano Letters*., vol. 6, no. 6, p. 1121-1125, 2006.

[77] A. M. Schrand, L. Dai, J. J. Schlager, S. M. Hussain E. Osawa, "Differential biocompatibility of carbon nanotubes and nanodiamonds*", Diamond and related materials*., vol. 16, issue. 12, p. 2118-2123, 2007.

[78] Y. S. Lee, M. Mrksich, "Protein chips: from concept to practice", *Trends in Biotechnology*., vol. 20, 2002.

[79] T. Laurila, "Hybrid carbon nanomaterials for electrochemical detection of biomolecules," *Physica Scripta*, vol. 90, no. 9, 2015.

[80] T. Laurila, A. Rautiainen, S. Sintonen, H. Jiang, E. Kaivosoja, and J. Koskinen, "Diamond-like carbon (dlc) thin film bioelectrodes: Effect of thermal posttreatments and the use of ti adhesion layer," *Materials Science and Engineering*: C, vol. 34, p. 446–454, 2014.

[81] J. Zang, Y. Wang, S. Zhao, L. Bian, and J. Lu, "Electrochemical properties of nanodiamond powder electrodes," Diamond and related materials, vol. 16, no. 1, p. 16–20, 2007.

[82] J. M. Halperna, S. X. Greg, P. S. Bryan, T. H. Cynthia, "Diamond electrodes for neurodynamic studies in Aplysia californica", *Diamond related materials*., vol. 15, issues. 2-3, p. 183-187, 2006.

[83] C. Prado, G. U. Flechsig, P. Gründler, J. S. Foord, "Electrochemical analysis of nucleic acids at boron-doped diamond electrodes", *Analyst.,* vol. 127, issue 3, p. 329-332, 2002.

[84] L. Reimer, “Scanning Electron Microscopy”, Springer Science and business, USA, 1998.

[85] B. Kharisov, O. V. Kharissova, U. O. Mendez, Handbook of less-common nanostructures”, CRC press, 2012.

[86] J. E. Crowell, “Chemical methods of thin film deposition: Chemical vapor deposition, atomic layer deposition, and related technologies”, *J. of vacuum science and tech*., vol. 21, S88, 2003.

[87] S. A. Skoog, W. Elam, R. J. Narayan, “Atomic layer deposition: medical and biological applications”, *International materials reviews*, vol. 58, issue 2, p. 113-129, 2013.

[88] A. L. Yarin, “Drop Impact Dynamics: Splashing, Spreading, Receding, Bouncing.”, *Annu. Rev. Fluid Mech*., vol. 38, p. 159–192, 2006.

[89] A. G. Emslie, F. T. Bonner, L. G. Peck, “Flow of viscous liquid on a rotating disk”, *Journal of applied physics* vol. 29, issue 5, p. 858, 1958.

[90] Y. Hong, H. Kim, G. Lee, “Controlled two-dimensional distribution of nanoparticles by spin-coating method”, *Applied physics letters*, vol. 80, issue 5, 2002.

[91] M. P. Aleksandrova, “Improvement of the Electrical Characteristics of Polymer Electroluminescent Structures by Using Spray-Coating Technology.” *Journal of Coating Technology,* vol. 9, p. 157–161, 2012.

[92] K. D. Vernon-Parry, "Scanning electron microscopy: an introduction", *Elsevier,* vol.13, issue.4, p.40-44, 2000.

[93] W. Zhou, Z. L. Wang, “Scanning Microscopy for Nanotechnology”, *Springer publication, USA,* 2007.

Appendix

Table A1**:** *Specific characteristics of DND Carbodeon uDiamond®used in experimental section*

Specific Characteristics	**Carbodeon uDiamond®**
Nanodiamond crystal size	4.2 ± 0.5 nm
Nanodiamond content	≥ 97 wt.%
Oxidisable carbon content	≤ 2.5 wt.%
Metallic incombustible impurity content	≤ 1.2 wt.%
Crystal lattice constant	0.3573 ± 0.0005 nm
pH stability of dispersion	3-6
Concentration of nanodiamonds in dispersion	5 wt. %
Zeta potential	positive

Table A2: *Details of parts of the automated spray coater and place of purchase*

Part details (and product number)	**Place of purchase**
3D printer (232/3dprintersonlinestore.com)	3D printers online store
Nozzle (TPU650017-SS)	Spraying Systems Oy
Viton tubes (228-0387)	VWR online shop
Ball valve	Hydromarket shop
Electrical valve	
Air tubes	
Liquid vessel	
Connectors and fittings	